Physics-Guided Deep Learning Model for Daily Groundwater Table Maps Estimation Using Passive Surface-Wave Dispersion

José Cunha Teixeira, Ludovic Bodet, Agnès Rivière, Amélie Hallier, Alexandrine Gesret, Marine Dangeard, Amine Dhemaied, Joséphine Boisson Gaboriau

Water Resources Research

RESEARCH ARTICLE
10.1029/2024WR037706

Special Collection:
Advances in Machine Learning for Earth Science: Observation, Modeling, and Applications

Physics-Guided Deep Learning Model for Daily Groundwater Table Maps Estimation Using Passive Surface-Wave Dispersion

José Cunha Teixeira[1,2], Ludovic Bodet[1], Agnès Rivière[3], Amélie Hallier[2], Alexandrine Gesret[3], Marine Dangeard[2], Amine Dhemaied[2], and Joséphine Boisson Gaboriau[2]

[1]CNRS, EPHE, UMR 7619 METIS, Sorbonne Université, Paris, France, [2]SNCF Réseau, Saint-Denis, France, [3]Geosciences Department, Mines Paris—PSL, PSL University, Paris, France

Key Points:

- Estimating groundwater table (GWT) maps from seismic dispersion measurements using deep learning
- Understanding the spatial and temporal dynamics of the GWT with high resolution
- Using the GWT geometry and dynamics to constrain the geological model of the site

Correspondence to:
J. Cunha Teixeira,
jose.teixeira@sorbonne-universite.fr

Citation:
Cunha Teixeira, J., Bodet, L., Rivière, A., Hallier, A., Gesret, A., Dangeard, M., et al. (2025). Physics-guided deep learning model for daily groundwater table maps estimation using passive surface-wave dispersion. *Water Resources Research*, *61*, e2024WR037706. https://doi.org/10.1029/2024WR037706

Received 8 APR 2024
Accepted 6 JAN 2025

Author Contributions:
Conceptualization: José Cunha Teixeira
Formal analysis: Agnès Rivière
Funding acquisition: Amine Dhemaied, Joséphine Boisson Gaboriau
Methodology: José Cunha Teixeira, Ludovic Bodet, Agnès Rivière
Project administration: Amélie Hallier, Amine Dhemaied, Joséphine Boisson Gaboriau
Software: José Cunha Teixeira
Supervision: Ludovic Bodet, Agnès Rivière, Amélie Hallier, Alexandrine Gesret, Marine Dangeard, Amine Dhemaied, Joséphine Boisson Gaboriau
Validation: José Cunha Teixeira
Visualization: José Cunha Teixeira

Abstract Monitoring groundwater tables (GWTs) remains challenging due to limited spatial and temporal observations. This study introduces an innovative approach combining an artificial neural network, specifically a multilayer perceptron (MLP), with continuous passive Multichannel Analysis of Surface Waves (passive-MASW) to construct GWT depth maps. The geologically well-constrained study site includes two piezometers and a permanent 2D geophone array recording train-induced surface waves. At each point of the array, dispersion curves (DCs), displaying Rayleigh-wave phase velocities (V_R) over a frequency range of 5–50 Hz, were measured daily from December 2022 to September 2023, and latter resampled over wavelengths from 4 to 15 m, to focus on the expected GWT depths (1–5 m). Nine months of daily V_R data near one piezometer, spanning both low and high water periods, were used to train the MLP model. GWT depths were then estimated across the geophone array, producing daily GWT maps. The model's performance was evaluated by comparing inferred GWT depths with observed measurements at the second piezometer. Results show a coefficient of determination (R^2) of 80% at the training piezometer and of 68% at the test piezometer, and a remarkably low root-mean-square error (RMSE) of 0.03 m at both locations. These findings highlight the potential of deep learning to estimate GWT maps from seismic data with spatially limited piezometric information, offering a practical and efficient solution for monitoring groundwater dynamics across large spatial extents.

Plain Language Summary This study combines deep learning with seismic ambient noise measurements to infer and monitor groundwater table (GWT) depths. The study site includes two piezometers and a sensor array that captures seismic waves induced by passing trains, providing daily seismic velocity measurements. An artificial neural network was trained using GWT depth data from one piezometer and seismic data collected at the same location. The trained model was then applied to estimate GWT depths across the entire sensor array, generating daily maps. The model's accuracy achieves a coefficient of determination (R^2) of 80% around the training piezometer, and 68% around the test piezometer. Estimation errors are also remarkably low, with a root-mean-square error (RMSE) of just 0.03 m at both locations. This research demonstrates the effectiveness of deep learning in estimating GWT depths from passive surface-wave data. It offers a practical tool for understanding underground water dynamics, improving water resource management, and environmental hazard assessment. Notably, this method enables efficient groundwater monitoring over large areas using limited data from a single piezometer.

1. Introduction

Groundwater (GW) systems are in dynamic balance between climatic forcing and human pressure. They play a pivotal role in addressing various water resource management and civil engineering matters. Monitoring the dynamics of groundwater table (GWT) geometry is essential for evaluating the resilience and quality of aquifers, predicting water availability, and allowing for sustainable extraction and use, particularly during extreme floods and droughts. Additionally, this understanding proves equally crucial for identifying high-risk infrastructures susceptible to GW-induced natural hazards. In fact, waterlogging events, landslides (Panda et al., 2022; Rahardjo et al., 2010), and sinkholes (Gutiérrez et al., 2014; Parise, 2019; Waltham et al., 2004; Xiao et al., 2020) are potential threats that can be anticipated and mitigated more effectively by incorporating knowledge of the dynamics of GWTs.

Writing – original draft: José Cunha Teixeira, Agnès Rivière
Writing – review & editing: José Cunha Teixeira, Ludovic Bodet, Agnès Rivière, Amélie Hallier, Alexandrine Gesret, Marine Dangeard, Joséphine Boisson Gaboriau

GWTs evolve beneath our feet and still represent a terra incognita (Kleinhans, 2005). The assessment of their geometry and dynamics remains a scientific barrier to be lifted. While piezometers can locally measure GWT depths with high precision and accuracy, it is important to acknowledge that their deployment is often spatially limited, resulting in sparse estimations across larger areas. To reduce this limitation, GWT maps are often interpolated from piezometric data, through techniques such as linear estimators and kriging (Maillot et al., 2019), and represent an important tool for hydrogeologists and civil engineers. While interpolation techniques offer unbiased results for GWT geometry, they do not account for the soil spatial heterogeneity between piezometers and are limited by the spatial distribution and number of piezometers. The effectiveness of the interpolation is contingent on the availability and strategic placement of these monitoring points, impacting the overall accuracy and reliability of the generated GWT maps.

One effective solution to address this limitation involves the conversion of lithofacies into hydrofacies information to constrain GWT map interpolations and simulations (Dagan, 1982; Tsai & Li, 2008). The integration of geophysical data can significantly enhance hydrological knowledge by providing spatial information where conventional hydrological measurement techniques are limited (Dafflon et al., 2009). Time-lapse geophysical methods, offer real-time data on changes in subsurface properties, aiding in the characterization of GWT geometry and the identification of spatial variability and temporal trends (Dangeard et al., 2021; Hermans et al., 2023). Methods such as ground-penetrating radar (GPR), induced polarization, self-potential, and resistivity, use the electrical and magnetic properties of the near-surface and are relevant in assessing soil water content (Garambois et al., 2002; Jougnot et al., 2015; Klotzsche et al., 2018; Loeffler & Bano, 2004; Samouëlian et al., 2005). However, they tend to be ineffective in very electrically conductive or resistive environments. Active seismic approaches, such as seismic reflection, refraction (Whiteley et al., 2020) and Multichannel Analysis of Surface Waves (MASW, Park et al., 1999) have been successfully used for water content monitoring (Bergamo et al., 2016; Lu, 2014) and GWT geometry characterization (Dangeard et al., 2021; Pasquet, Bodet, Dhemaied et al., 2015; Pasquet, Bodet, Longuevergne, et al., 2015). They mostly rely on the study of the pressure-(P) and shear-(S) wave velocities (V_P and V_S) to estimate V_P/V_S or Poisson's ratios (Biot, 1956a, 1956b), which are sensitive indicators of fluid presence. However they face limitations due to the difficulty to regularly deploy active sources in adverse conditions, making continuous characterizations impossible.

Passive seismic methods, use continuous and coherent ambient seismic noise generated by natural or anthropogenic activities. They rely on seismic interferometry and consist in the Green's function retrieval by cross-correlation between recording sensors pairs to provide a characterization of the propagation medium (Aki, 1957; Derode et al., 2003; Larose et al., 2015; Wapenaar, 2004; Wapenaar, Draganov, et al., 2010; Wapenaar, Slob, et al., 2010; Weaver & Lobkis, 2004). Some approaches monitor the relative temporal variation of seismic velocities for specific wavefronts (referred to as dv/v) between pairs of sensors, and have put on evidence a clear correlation with GWT depth variations (Barajas et al., 2021; Clements & Denolle, 2018; Garambois et al., 2019; Gaubert-Bastide et al., 2022; Grêt et al., 2006; Kim & Lekic, 2019; Lecocq et al., 2017; Mao et al., 2022; Qin et al., 2022; Voisin et al., 2016, 2017; S. Zhang et al., 2023). Although this method is able to correlate the seismic velocity variations and GWT depth variation maps (Gaubert-Bastide et al., 2022), it provides limited information about the aquifer geometry and the proper GWT depth.

Another employed approach is the passive-MASW, an extension of the standard active-MASW. This technique relies on the propagation of ambient Rayleigh-waves, induced by cars or trains, through linear geophone arrays to characterize the near-surface and has found application in various civil engineering contexts, both sporadically in time with 1D setups (Cheng et al., 2015, 2016; Czarny et al., 2023; Mi et al., 2022, 2023; Park & Miller, 2008; Quiros et al., 2016; Rezaeifar et al., 2023; You et al., 2023), and for continuous sinkhole monitoring with 2D configurations (Bardainne, Cai, et al., 2023; Bardainne & Rondeleux, 2018; Bardainne, Tarnus, et al., 2023; Bardainne, Vivin, & Tarnus, 2023; Bardainne et al., 2022; Rebert, Bardainne, Allemand, et al., 2024, Rebert, Bardainne, Cai, et al., 2024; Tarnus et al., 2022a, 2022b). The characterization process is based on the analysis of dispersion curves (DCs), which depict the fluctuation of Rayleigh-wave phase velocity (V_R) across frequencies, along the linear arrays. V_R variation over frequency, seen in DCs, is closely linked to the medium's V_S variation over depth, which is influenced by the water content (Solazzi et al., 2021). Nevertheless, the shift from DCs to ground models incorporating water saturation profiles and GWT depth information involves intricate inversion operations, combining geophysical and hydrogeological data, that are still under development.

Piezometers offer valuable but localized and sparse hydrogeological data, while geophysical methods help in interpolating and extrapolating this information. However, geophysical methods often lack direct connections to hydrogeological principles. More recently, machine learning (ML) and deep learning (DL) methodologies have gained significant prominence in hydrology and water resource applications (see Tripathy & Mishra, 2024 for an overview on DL usage in hydrology). More specifically, physics-guided models, incorporating geophysical knowledge into ML or DL models, were used to effectively handle and uncover hidden patterns in complex and high-dimensional data sets, and served as a bridge between hydrogeology and geophysics. Abi Nader et al. (2023) combined ML and seismic monitoring to appraise GWT depths with great precision, using raw seismic noise records. Cai et al. (2022) was able to estimate GWT depths with more accuracy with a physics-guided DL model than with a pure DL model, using water balance equations as a physical constraint.

This study leverages a geologically well constrained sinkhole-affected site equipped with a dense geophone array and two piezometers. It offers almost a year of observed passive seismic data, revealing temporal trends that could be correlated with the GWT depth seasonal variations. The objective is to demonstrate the utility of DCs, obtained through passive seismic methods, in monitoring GWT depths. We couple passive-MASW and a simple artificial neural network, more precisely a Multilayer Perceptron (MLP), to estimate daily GWT maps from a single piezometer. After introducing the test site and providing a comprehensive overview of the passive-MASW survey geometry and data, we give a description of the method employed for building, training and testing the MLP. Subsequently, we showcase the generated GWT maps resulting from the application of this method, discuss the hydrogeological implications, and explore the limitations associated with such approach.

2. Study Site and Data

2.1. A Sensitive but Well Constrained Site

The study site is located along a railway line in the Grand-Est region of France (see Figures 1a and 1b) at the eastern edge of the Paris Basin. The site features a stratigraphic composition dominated by a 75-m-thick cover formation, consisting of the middle and lower Muschelkalk layers. This cover formation is composed with alluvium, impermeable clays, and marls, all dating back to the Middle Triassic period, and is underlayed by the lower Triassic sandstone (LTS) formation. The subsurface aquifer has not been described at the site, only a large GWT map of the deeper LTS confined aquifer, dating from 2010, is available at the Lorraine region scale (Nguyen-Thé et al., 2010).

Between 1989 and 2017, this railway site has encountered several instances of sinkhole dropouts, particularly impacting the integrity of the railway on the southwest side toward the bridge (see Figure 1c). These sinkholes are attributed to the dissolution of gypsum veins within the marl layer. Consequently, a cement-based grout was injected at a depth of 20 m in the soil to reinforce the structure in 2018. Five auger drilling tests with depths up to 20 m were conducted in December 2022 with the aim of detecting potential eventual cavities, as depicted in Figure 1c. These tests did not reveal cavities, and facilitated a visual characterization of the various layers of the near-surface (see Figure 1d). An approximately 10 m-thick layer of alluvium, consisting of a mixture of sand and gravel, appears to overlay a denser layer of gray clays and a highly compacted marl layer. Additionally, a sandy gravely clay layer was found between depths of 5 and 10 m, at one of the five drillings (see Figure 1d). This observations align coherently with the expected geological composition of the top of middle and lower Muschelkalk cover layer.

The studied subsurface aquifer is located above the gray clay aquitard formation, within the alluvium and sandy gravely clay layers, which are hydraulically connected (see Figure 1d). However, information on its connectivity with the LTS aquifer is not available, therefore, is not considered here.

To effectively address and mitigate the risks posed by sinkholes, a continuous ground monitoring, through passive-MASW using seismic noise induced by trains (Bardainne, Cai, et al., 2023; Bardainne & Rondeleux, 2018; Bardainne, Tarnus, et al., 2023; Bardainne, Vivin, & Tarnus, 2023; Bardainne et al., 2022; Rebert, Bardainne, Allemand, et al., 2024; Rebert, Bardainne, Cai, et al., 2024; Rebert et al., 2023; Tarnus et al., 2022a, 2022b), and combined with two piezometers has been established as the best approach in late 2020. Following the installation of the piezometers in late 2022, this study covers a 9-month period, from 30 December 2022, to 3 September 2023, encompassing the aquifer's response under both low and high water period conditions.

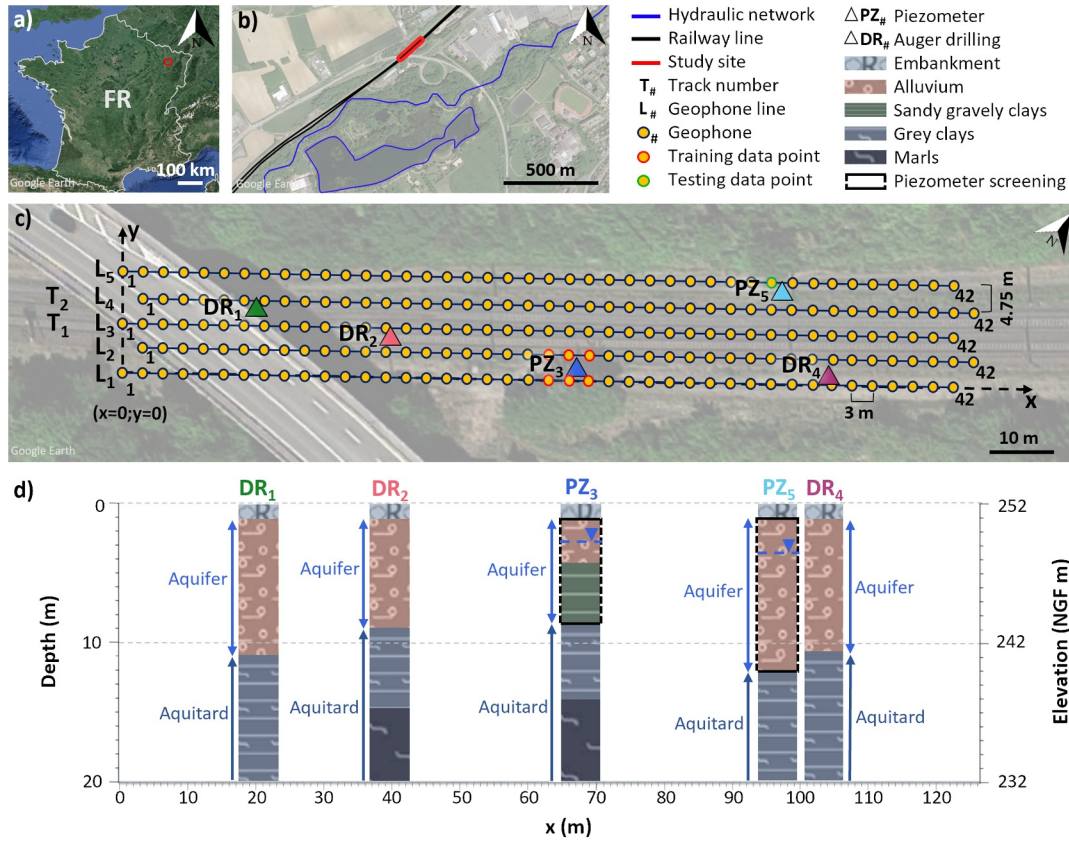

Figure 1. (a and b) Location map of the site, and close hydraulic networks. (c) Experimental design of the study site showing the five lines (L_1 to L_5) of 42 vertical component geophones (yellow dots), planted parallel to the railway tracks, and the track numbers (T_1 and T_2). x and y correspond to the distance parallel and perpendicular to the railway tracks, respectively, and point ($x = 0; y = 0$) is at geophone 1 of array line 1 ($L_1 - P_1$). Data points used for training and testing the MLP are colored in red around piezometer PZ_3, and green close to piezometer PZ_5, respectively. DR_1, DR_2, and DR_4 correspond to auger drilling locations without piezometers. (d) Lithographic log at the 5 drillings. The lithology at the site consists of an 10 m thick alluvial layer, composed of sand and gravel, overlying a denser section of gray clays and a highly compacted marl layer with gypsum veins. However, at PZ_3, a distinct layer of sandy gravely clays is present between depths of 5 and 10 m. The studied aquifer is located within the alluvial, and sandy gravely clay layers, above the impermeable gray clay layer. The piezometer at PZ_3 was screened between depths of 1–8 m, while piezometer PZ_5 was screened between 1 and 11 m. Both piezometers were sealed at the top and bottom with bentonite to ensure proper isolation.

2.2. Passive-MASW

The seismic dispersion data was originally acquired and processed by Bardainne and Rondeleux (2018). Daily DCs were measured using a passive-MASW approach (Bardainne, Cai, et al., 2023; Bardainne, Vivin, & Tarnus, 2023; Cheng et al., 2015, 2016; Czarny et al., 2023; Mi et al., 2022; Park & Miller, 2008; Quiros et al., 2016; Rezaeifar et al., 2023; Tarnus et al., 2022b; You et al., 2023), which combines seismic interferometry (Bensen et al., 2007) with traditional MASW (Bergamo et al., 2012; Bohlen et al., 2004; L. Socco & Strobbia, 2004; L. V. Socco et al., 2010; Pasquet & Bodet, 2017).

Since September 2020, seismic noise induced by train passages, has been continuously recorded using five uniform linear arrays of vertical component geophones (L_1 to L_5 on Figure 1c). Each linear array has a length of 123 m and is equipped with 42 3-m spaced geophones. The geophones were strategically positioned along the rail track, either on the cess (i.e., the track side) for linear arrays L_1 and L_5, or on the ballast for L_2, L_3, and L_4. Note that our experience has shown that the ballast does not significantly affect the quality of the data.

For each day, passage events were automatically detected by taking advantage of their high signal-to-noise ratio. Then, based on the assumption that trains act as permanent and well-localized moving sources (Bardainne et al., 2022; Rebert, Bardainne, Allemand, et al., 2024; Rebert, Bardainne, Cai, et al., 2024; Rebert et al., 2023),

specific time intervals were selected. These intervals correspond to moments when the train is outside the seismic array but still within a range that maintains sufficient seismic energy, and the induced waves propagate in alignment with all the geophones along the geophone lines. In the literature, various techniques have been used as automatic segment selection tools. These include Frequency-Wavenumber (FK)-based data selection (Cheng et al., 2018), data selection in the Tau-p domain (Cheng et al., 2019), beamforming techniques (Ning et al., 2022), and covariance matrix methods for train localization in time and space (Rezaeifar et al., 2023). However, the specific selection method used by Bardainne and Rondeleux (2018) is not known to the authors.

The selected time intervals were then divided into overlapping short segments of a few seconds each (usually around 10 s), and cross-correlation was applied on every geophone pair. This process forms a virtual shot-gather for each segment, illustrating the propagation of seismic waves from the first sensor (acting as the virtual source) to the subsequent sensors. To improve the reliability of the data, virtual-shot gathers resulting from all segments of multiple trains passages (approximately 40 per day) were stacked together in the time-domain. This stacking process enhances the signal-to-noise ratio, as random noise tends to cancel out while the consistent seismic signals reinforce each other. Our experience indicates that even a relatively small number of train passages can provide sufficient data for effective analysis.

Finally, a MASW window of 21 m (over 8 geophones) with a moving step of 3 m (1 geophone interval) was used to extract surface-wave dispersion curves from the stacked virtual shot-gathers along each geophone line. Within the sliding MASW window shot-gathers were transformed from the distance-time (x, t) domain into dispersion images in the frequency-phase velocity (f, V_R) domain using a phase-shift transform (Park et al., 1999), and the fundamental propagation mode DC was automatically picked between 5 and 50 Hz (Tarnus et al., 2022b). Each DC was then positioned at its associated MASW window center to construct the five V_R profiles between 10.5 and 115.5 m.

In parallel, Spectral Analysis of Surface Waves (SASW, Nazarian et al., 1983) was also used to construct horizontal maps of V_R, for frequencies ranging from 5 to 50 Hz, between pairs of geophones. The resulting velocities were combined with the velocities estimation from passive-MASW to construct a complete V_R cube, through an Eikonal based tomography procedure, between 0 and 126 m. Finally, at each geophone line y-position, DCs were extracted from the data cube at each geophone location, and at the limits of the array. This results in a rectangular configuration of 43 data points per geophone line, as they are alternatively shifted by one geophone (see Figure 1c).

The daily DCs estimated at each array point, covering a frequency range from 5 to 50 Hz, were resampled in wavelength $\lambda = V_R/f$, where f is the frequency, within the range of 4–15 m, and a step of 0.5 m. V_R variation over frequencies or wavelengths, seen in DCs, is linked to the medium's V_S variation over depth. However, it's crucial to note that this transformation is nonlinear. Yet, wavelength resampling offers a more accurate link to depth in comparison to frequencies, enabling precise targeting of the first meters of the near-surface. Typically, the maximum sensitivity depth corresponds to approximately a half or one-third of the wavelength (Foti et al., 2018). Therefore, this resampling primarily targets depths ranging from 1.5 to 5 m, where the GWT is expected.

Figure 2 shows every estimated daily DC, from 30 December 2022, to 3 September 2023, sampled over frequencies and wavelengths, close to PZ_3 at point 23 of geophone line 1 (L_1-P_{23}), and close to PZ_5 at point 33 of geophone line 5 (L_5-P_{33}) (see Figure 1c). In Figure 3, examples of V_R pseudo-sections showcase the DCs sampled over wavelengths along the 5 linear arrays, on 1 April 2023, and 1 July 2023, at high and low water periods, respectively (see Figures 4a and 4b). V_R pseudo-sections over frequencies version is shown in Figure A1 of Appendix A. Figures 2 and 3 reveal a spatial and temporal evolution of V_R that could be correlated with GWT geometry and dynamics. This indicates the potential utility of employing this method for the ongoing monitoring purposes.

2.3. Piezometers

Both piezometers were equipped on 30 December 2022, at two of the five drilling locations, separated by approximately 40 m, and have been recording daily GWT depths over time (see PZ_3 and PZ_5 in Figure 1c). The altitude of both piezometers is identical (252 m NGF), and the screened was applied over the studied subsurface aquifer (see Figure 1d), within the alluvium and sandy gravely clay layers. PZ_3 was screened between depths of 1–8 m, while piezometer PZ_5 was screened between 1 and 11 m. The top and bottom of the piezometers were sealed with bentonite.

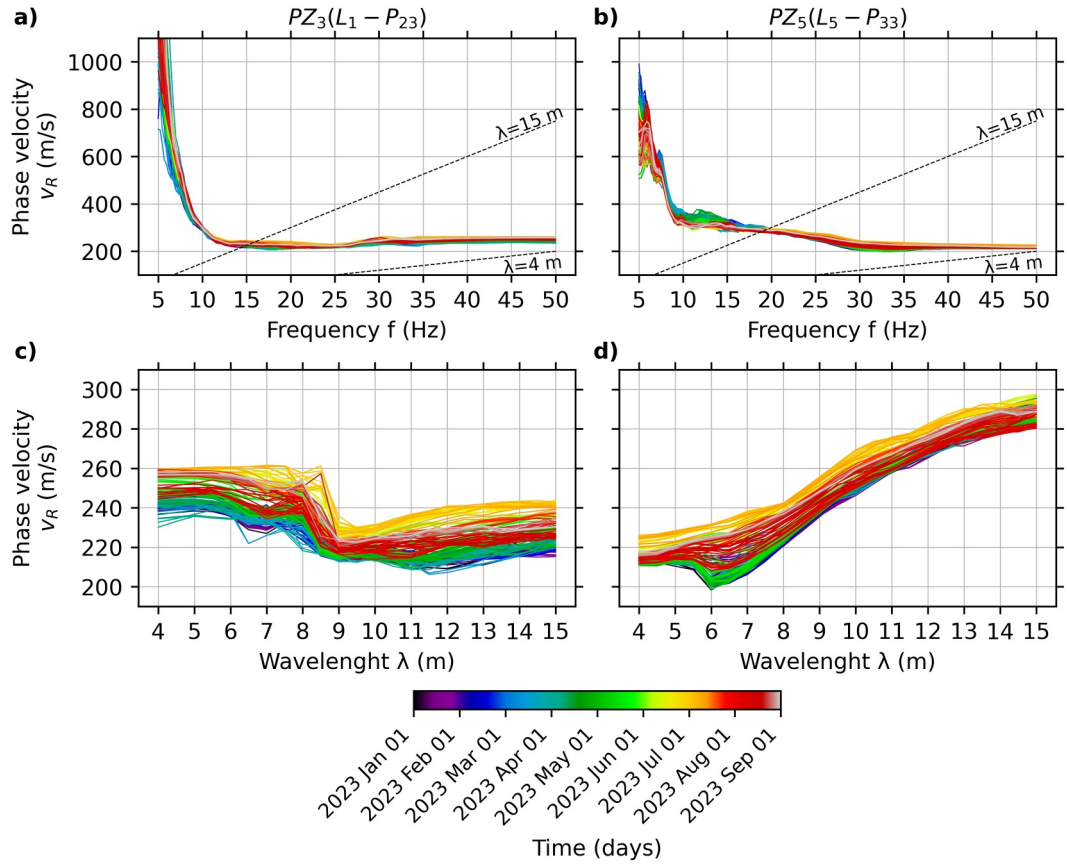

Figure 2. Time-series of raw dispersion curves over frequencies measured (a) at seismic array point L_1-P_{23}, close to piezometer PZ_3, and (b) at seismic array point L_5-P_{33}, close to piezometer PZ_5. Resampled dispersion curves over wavelengths, ranging from $\lambda = 4$ to $\lambda = 15$ m, (c) at seismic array point L_1-P_{23}, close to piezometer PZ_3, and (d) at seismic array point L_5-P_{33}, close to piezometer PZ_5 (see Figure 1c).

GWT depth data at PZ_3 and PZ_5 is presented in Figures 4a and 4b. The two piezometers display distinct hydrological responses. PZ_3 recorded GWT fluctuations between 1.75 and 3 m, while PZ_5 ranged from 2.5 to 3.5 m. PZ_3 demonstrated greater sensitivity and amplitude variations than PZ_5. This disparity can be attributed to the lithology heterogeneity and the aquifer geometry. The subsurface aquifer at the PZ_3 location consists of both alluvium and a less permeable sandy gravelly clay layer, whereas at PZ_5, only alluvium is present (see Figure 1d).

2.4. Data Correlation

Figures 4c and 4d illustrate the temporal evolution of V_R across all wavelengths at the piezometers locations. We observe a correlation between the variation of the DCs and the observed GWT depth at array points near each piezometer (see Figures 2c and 2d). An increase in GWT depth is associated with a general increase in V_R, while a decrease in GWT depth corresponds to a reduction in V_R. This correlation is evident across all wavelengths at varying amplitudes, as shown in Figures 4c and 4d, and becomes even more pronounced when focusing on specific wavelengths in Figures 4e and 4f. The observed relationship between GWT depths and V_R is indicative of the influence of groundwater dynamics on the spatial distribution and temporal evolution of V_R. Given the observed correlation between DCs and GWT depths at these piezometers, it is plausible to hypothesize that this correlation persists across all points along the seismic array. It is worth noting that the steep change in V_R at $\lambda = 8$ m observed in Figures 2c and 4c could correspond to the GWT depth at PZ_3. However, conclusive determination requires inversion of the DCs into V_S over depth models.

We suggest training an artificial neural network with seismic and GWT depth data from PZ_3, as it exhibits the most pronounced responsiveness among the two piezometers. The objective is to translate the DCs into GWT depths, enabling the estimation of GWT maps across the entire array.

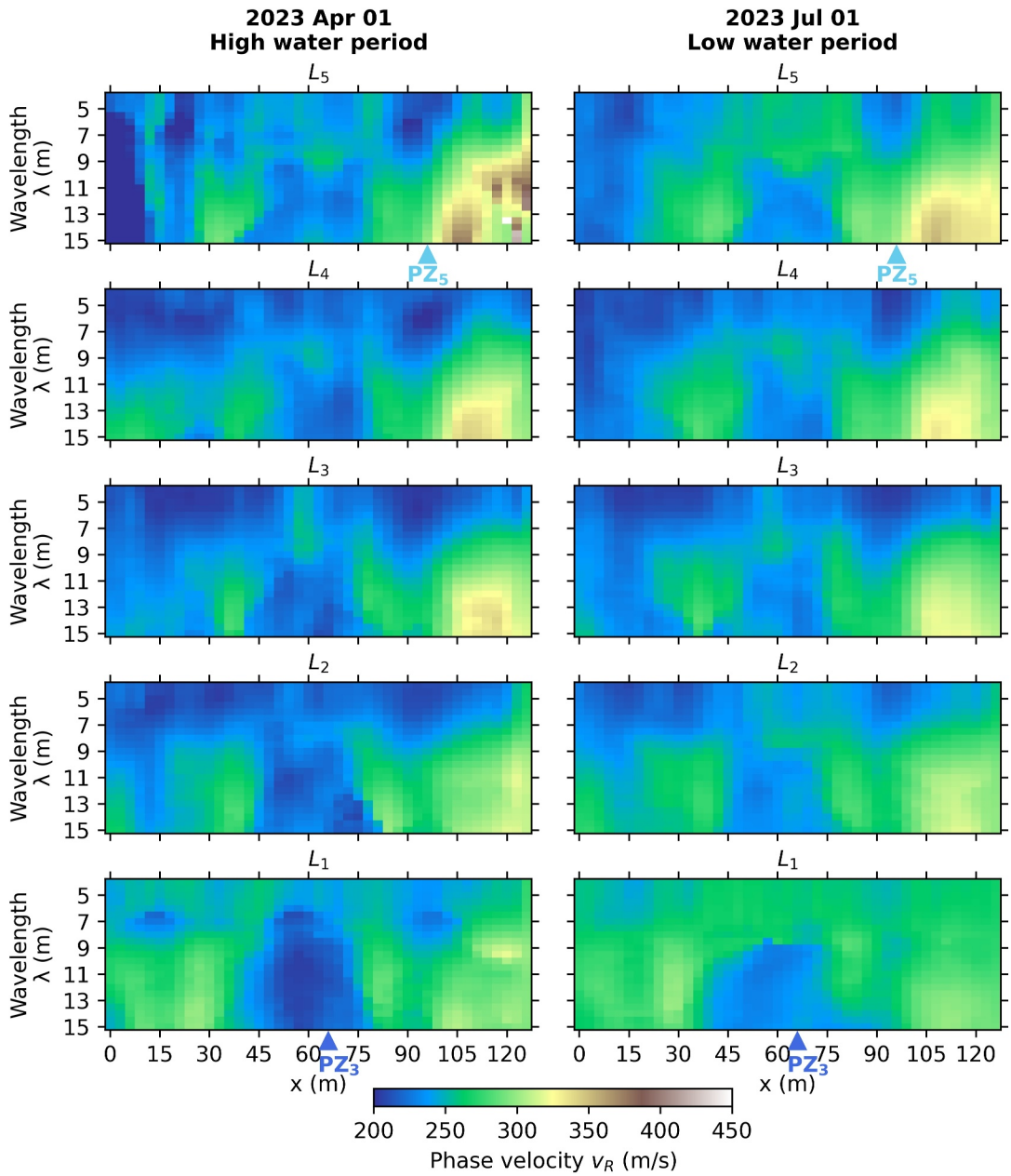

Figure 3. V_R pseudo-sections over wavelengths for the 5 linear geophone arrays (L_1 to L_5) (left) at a high water period on 1 April 2023, and (right) at a low water period on 1 July 2023. Positions of piezometers PZ_3 and PZ_5 are represented by the blue triangles on pseudo-sections L_1 and L_5, respectively.

3. Methods

3.1. Multilayer Perceptron Architecture

In this study, an MLP is used as a regression tool for estimating a GWT depth from each DC, at several seismic array points and times. The MLP is the most basic feedforward artificial neural network and consists of multiple layers of fully connected neurons, comprising an input layer, one or more hidden layers, and an output layer (Goodfellow et al., 2016; Murtagh, 1991; Rosenblatt, 1958). The use of an MLP allows for complex non-linear mappings between inputs and outputs, making it particularly well-suited for capturing intricate relationships within numerical data sets. It has been widely used in hydrogeology in numerous applications (Altunkaynak & Strom, 2009; Boucher et al., 2020; Kawo et al., 2024; C. Zhang et al., 2022).

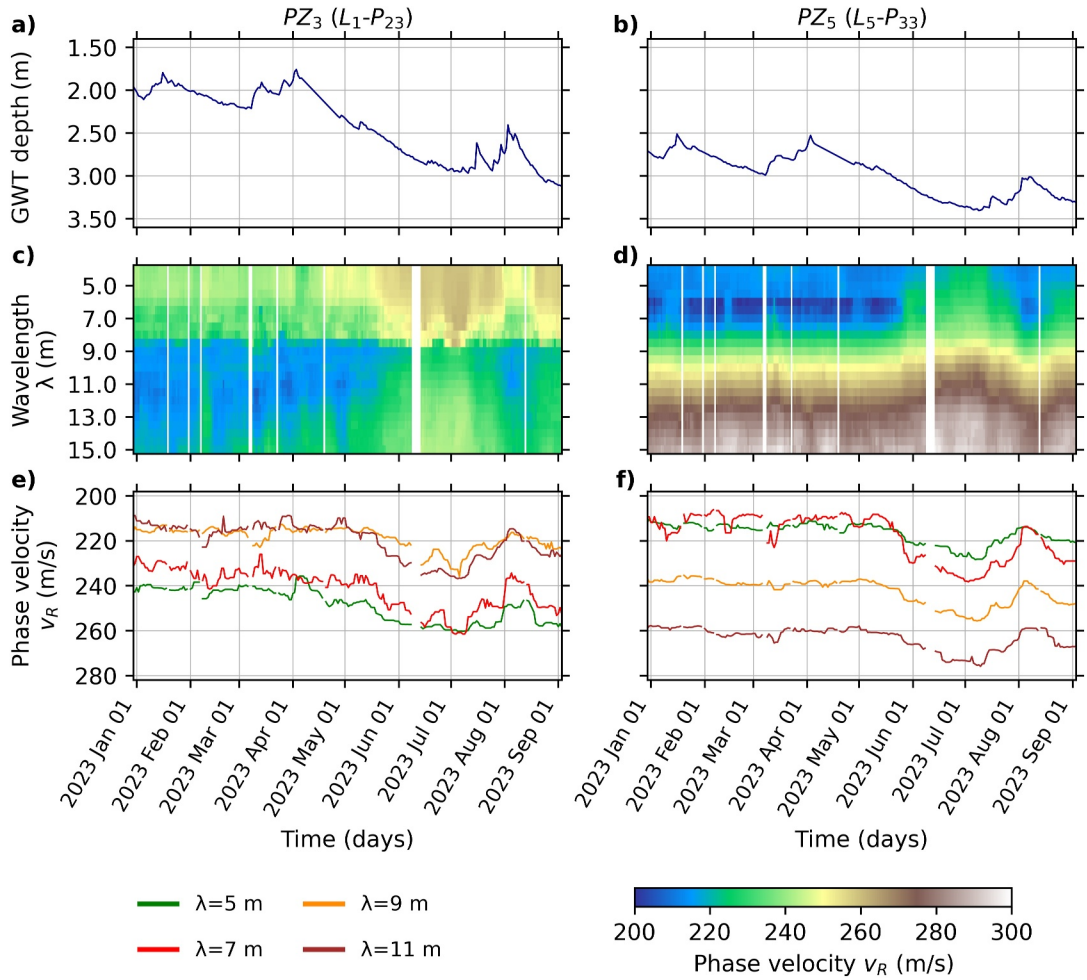

Figure 4. (a and b) Recorded GWT depths between 30 December 2022, and 3 September 2023, at PZ_3 and PZ_5. (c and d) V_R over wavelengths evolution over the same time period at seismic array points L_1-P_{23}, close to PZ_3, and L_5-P_{33}, close to PZ_5. (e and f) V_R at wavelengths 5, 7, 9, and 11 m evolution over the same time period at seismic array points L_1-P_{23}, close to PZ_3, and L_5-P_{33}, close to PZ_5.

Given the relatively small size of our data set, we opted for a small MLP to mitigate the risk of overfitting. We experimented with architectures ranging from two to three layers, with varying numbers of neurons per layer (8, 16, 32, and 64), and observed that increasing the depth beyond two layers did not significantly improve validation performance and often led to overfitting, while reducing the number of neurons resulted in underfitting. We selected an MLP architecture with two hidden layers and 32 neurons per layer (see Figure 5), which provides a good trade-off between model complexity and generalization ability, as evidenced by its performance on the validation set (see Table 1).

The input and output layer sizes correspond to the number of features of the input and output data. For each estimation, a unique DC of V_R resampled over wavelengths ranging from 4 to 15 m and with a wavelength step of 0.5 m, is used as input, which can be seen a vector $\boldsymbol{x}$ of size $n = 23$. The output corresponds to a unique scalar y of an estimated GWT depth.

For each layer l, let $\boldsymbol{w}^{(l)}$ be a vector of weights, initially containing arbitrary values, and $\boldsymbol{b}^{(l)}$ a vector of constants called "bias." At the first hidden layer, the weighted sum $\boldsymbol{z}^{(1)}$ is computed for each neuron j over the k neurons of the layer, as

$$z_j^{(1)} = b_j^{(1)} + \sum_{i=1}^{n} w_{ij}^{(1)} x_i, \tag{1}$$

with each feature i over the n features of the input vector $\boldsymbol{x}$. Then, the vector $\boldsymbol{z}^{(1)}$ goes through a *Rectified Linear Unit* (*ReLu*) function introducing non-linearity to the model. The output $\boldsymbol{h}^{(1)}$ of the *ReLu* function is given by

$$h_j^{(1)} = ReLu\left(z_j^{(1)}\right) = \begin{cases} z_j^{(1)} & \text{if } z_j^{(1)} > 0, \\ 0 & \text{otherwise,} \end{cases} \tag{2}$$

for each neuron j over the k neurons of the first hidden layer.

At the second layer $l = 2$, the weighted sum $\boldsymbol{z}^{(2)}$ is

$$z_j^{(2)} = b_j^{(2)} + \sum_{i=1}^{k} w_{ij}^{(2)} h_i^{(1)}, \tag{3}$$

for each neuron j over the k neurons of the second layer, and with each neuron i over the k neurons of the previous first hidden layer. Again, the vector $\boldsymbol{z}^{(2)}$ goes through a *Rectified Linear Unit* function *ReLu*. The output $\boldsymbol{h}^{(2)}$ of the *ReLu* function is given by

$$h_j^{(2)} = ReLu\left(z_j^{(2)}\right) = \begin{cases} z_j^{(2)} & \text{if } z_j^{(2)} > 0, \\ 0 & \text{otherwise,} \end{cases} \tag{4}$$

for each neuron j over the k neurons of the second hidden layer.

Finally, the output $z^{(out)}$ of the *ReLu* function is given by

$$z_1^{(out)} = b_1^{(out)} + \sum_{i=1}^{k} w_{i1}^{(out)} h_i^{(2)}, \tag{5}$$

for the unique neuron of the output layer, and with each neuron i over the k neurons of the previous second hidden layer. Finally, $z^{(out)}$ goes through an *Identity* activation function *linear*, to obtain the estimated scalar value y:

$$y = linear\left(z^{(out)}\right) = z^{(out)}. \tag{6}$$

3.2. Data Preprocessing and Training

The MLP goes through a training phase to optimize its performance and enhance its ability to make accurate estimations. The training data involved daily measured DCs at specific seismic array points surrounding PZ_3 (L_1-P_{22}, L_1-P_{23}, L_1-P_{24}, L_2-P_{21}, L_2-P_{22}, and L_2-P_{23}) as inputs, and daily GWT depth observations at PZ_3 as expected outputs. Thus, for an unique daily GWT depth output, six different inputs are used, corresponding to the closest six points around the piezometer. Thanks to the similarity of the DCs at these points, this allows for a better spatial versatility of the model, and can be seen as data augmentation (Shorten & Khoshgoftaar, 2019). To facilitate the training phase, DCs are normalized by 2000 (i.e., around twice the maximum observed V_R) and GWT depths are in absolute numbers. The data collection spanned from 30 December 2022, to 3 September 2023, encompassing a total of 248 days. Days without data, due to technical issues, were excluded from the data set.

During the training process, weights and biases are refined to minimize the difference between estimated outputs and actual target values. The training begins with the presentation of the training data, with known input and outputs, to the MLP. Subsequently, the calculated errors of the resulting estimations, in terms of *root-mean-square error* (RMSE), are backpropagated through the network (Linnainmaa, 1976; Rosenblatt, 1958; Werbos, 1982). This involves adjusting the weights and biases in the opposite direction of the error gradient. In this study, the magnitude of these adjustments was determined by a stochastic gradient descent *Adam* optimization algorithm with a learning rate of 10^{-4} (Kingma & Ba, 2017). This iterative adjustment process was done until the MLP converged to a state where further refinement did not significantly improve its estimation capabilities. The

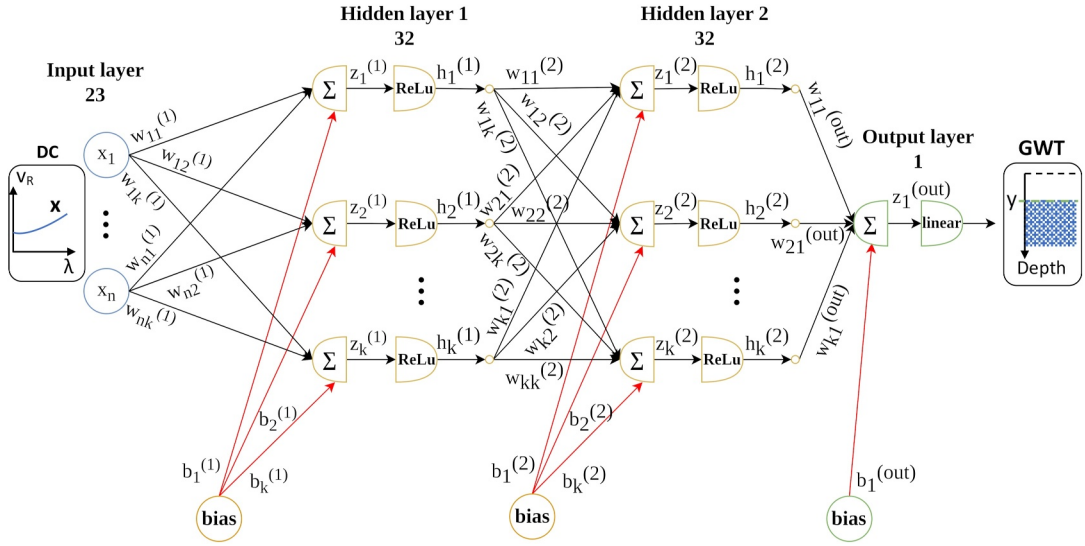

Figure 5. Multilayer perceptron comprising an input layer, two hidden layers, and an output layer. A DC (V_R over wavelength λ) is used as input to predict a GWT depth. The input vector $\boldsymbol{x}$ has $n = 23$ features, each hidden layer l has $k = 32$ neurons, and the output y is a scalar. $\boldsymbol{w}^{(l)}$ is a weight or leaning coefficient vector and $\boldsymbol{b}^{(l)}$ a vector of constants called "bias." *ReLu* and *linear* are the *Rectified Linear Unit* and *Identity* activation functions.

resulting trained MLP features optimized internal parameters, enabling it to generalize effectively to new, unseen data and deliver accurate estimations across diverse scenarios.

A maximum of 1,000 training epochs (i.e., iterations) with 2 samples per batch were done. Additionally, DCs at seismic array points surrounding PZ_5 (L_4-P_{31}, L_4-P_{32}, L_4-P_{33}, L_5-P_{32}, L_5-P_{33}, and L_5-P_{34}), as well as GWT depths at PZ_5 were used as a validation data set for "early stopping," limiting the number of epochs to 541, and avoiding the overfitting of the model (Tripathy & Mishra, 2024; Ying, 2019).

4. Results

Figure 6 compares the GWT depths observed at PZ_3 and PZ_5 with the estimations at seismic array points L_1-P_{23} close to PZ_3, and L_5-P_{33} close to PZ_5, between 30 December 2022, and 3 September 2023. As anticipated, the estimated and observed values at PZ_3, which was used in the training process, show close proximity (see Figures 6a and 6b), with an RMSE of 0.03 m and a *coefficient of determination* (R^2) of 80% (see Appendix D for definitions). Please note that this score could possibly be higher but is limited to able a great generalization of the model. While the model successfully captures the general patterns, it exhibits minor fluctuations that deviate from the observed values. However, the overall agreement between estimated and observed values underscores the model's capability to replicate the general trends associated with PZ_3.

Table 1
Performance Comparison of MLP Architectures With Varying Number of Layers and Neurons

		Training data set		Validation data set	
Neurons per layer	Epochs	RMSE	R^2	RMSE	R^2
(8, 8)	626	0.02	0.86	0.05	0.09
(16, 16)	504	0.02	0.86	0.03	0.43
(32, 32)	541	**0.03**	**0.80**	**0.03**	**0.68**
(64, 64)	617	0.02	0.88	0.06	−0.02
(8, 8, 8)	603	0.03	0.81	0.03	0.59
(16, 16, 16)	564	0.02	0.86	0.05	0.09
(32, 32, 32)	605	0.02	0.89	0.06	−0.13
(64, 64, 64)	543	0.02	0.87	0.10	−0.76

Note. The bolded values represent the MLP architecture with the most favorable results on the validation set.

The model also demonstrates its ability to accurately extrapolate and estimate GWT depths at PZ_5, a location not included in the training data set (see Figures 6c and 6d). It is important to note that while the piezometers in this study are relatively close to each other (around 40 m), they do not demonstrate the exact same behavior and GWT depth ranges. Specifically, the training data ranged between 1.75 and 3.10 m (see PZ_3 on Figure 6), but the model accurately inferred values around 3.5 m over the test data set (see PZ_5 on Figure 6). Overall, estimations for PZ_5 yield an RMSE of 0.03 m and an R^2 of 68%, suggesting a low level of estimation error and a high degree of accuracy. However, GWT depths are slightly underestimated by 25 cm between May and June 2023 and between August and September 2023. These errors could possibly be corrected by extending the time span of GWT depth data used for training, a limitation imposed by the time-frame of this research.

Figures 7b–7i show the inferred GWT maps, at the beginning of January, February, April, May, June, July, August, and September 2023. GWT depth evolution over time at the five drilling locations are highlighted in Figure 7a. The GWT maps exhibit a noticeable global variation, of approximately 1 m, between the high water period (April 2023) and the low water period (July 2023) (see Figure 8). Nevertheless, a spatial heterogeneity over x and y is evident, revealing zones with relatively shallow and deep GWT. The areas between $x = 30$ and $x = 60$m, encompassing PZ_3, and between $x = 80$ and $x = 90$ m, encompassing $PZ5$, demonstrate a shallow GWT from January to May 2023. However, a noticeable depth increase is observed during the summer months (June–August). In the central area of the map, a small high-depth zone with minimal variation over time, enclosed by a low-depth zone, can be noticed. Areas between $x = 20$ and $x = 30$ m, and between $x = 60$ and $x = 80$ m, exhibit relatively shallow GWT. Additionally, the zone between $x = 90$ and $x = 126$ m, which includes DR_4, displays a deeper GWT. For reference, this zone also registered the highest values of V_R (see Figure 2).

5. Discussion

5.1. Geologic Interpretation

Spatial and temporal variations in GWT depths observed in Figures 7 and 8 could be explained by differences in lithology over the studied site, effectively captured by seismic data. Areas exhibiting a consistent shallow GWT could be attributed to the presence of less permeable materials, such as clay, near to the surface. In such case, GW is impeded from infiltrating into the subsurface, contributing to the observed shallow GWT depths. Conversely, areas with a constant deep GWT may be associated with more permeable materials beneath alluvium.

Figure 9 shows the GWT cross-section traversing through all five drilling points, for different months along the year, with geological logs illustrating the nature of the encountered materials. As expected, the GWT is shallower and exhibits greater variation above the shallow sandy gravelly clay layer observed at PZ_3. Between DR_2 and PZ_3, close to DR_2, as well as between PZ_3 and PZ_5, there is a increase in the GWT depth, with a distinctive pinching point. This could be explained by a transition from highly impermeable to more permeable materials. All this suggests that zones $x = 30$ and $x = 60$ m, and between $x = 80$ and $x = 90$ m in a lesser degree, present a shallow clay layer.

This study represents a first approach attempting to confirm that the DCs are sensitive to temporal variations in GWT depths. However to further validate these permeability interpretations, it would be essential to conduct laboratory permeability tests on the collected samples to further substantiate the influence of lithological properties on groundwater dynamics.

5.2. Concordance With Inverted V_S Data

Pseudo-sections of V_R over wavelengths for the five geophone array lines, measured during the high water period (1 April 2023) and the low water period (1 June 2023), and displayed in Figure 2, were inverted into sections of V_S over depth (see Figure 10 and Figure C1 in Appendix C).

Remarkably, for the five sections, the estimated GWT depths align perfectly with a low-velocity layer for x between 30 and 80 m (blue on Figure 10), characterized by a low V_S between 200 and 250 m/s. Around $x = 60$ on L_1, this low-velocity layer is positioned just above the observed clay layer at drilling point PZ_3, and could correspond to saturated alluvium. This alignment supports the credibility of the method, as the MLP successfully estimated the depth of this layer despite the absence of direct depth information in the DCs used as input to the model.

Outside this area (x between 30 and 80 m), the relationship between a low V_S anomaly and the GWT depth is less evident. As expected, zones with higher V_S show a deeper GWT that seems to follow the geometry of a deep shallow low-velocity layer with an unclear delimitation. This zones align with the absence of the sandy gravely clay layer at 5 m depth, and could be explained by a deeper interface between alluvium and the impermeable underlying gray clay layer.

5.3. Inference Limitations

Artifacts exhibiting very shallow GWT estimations (between 0 and 1 m) and very deep GWT estimations (around 6 m) can be observed at the border of the maps, along geophone line L_5, between February and May 2023 (see Figures 7c–7e). Additionally, the area between $x = 0$ and $x = 15$ m, comprising DR_1, consistently exhibits

10.1029/2024WR037706

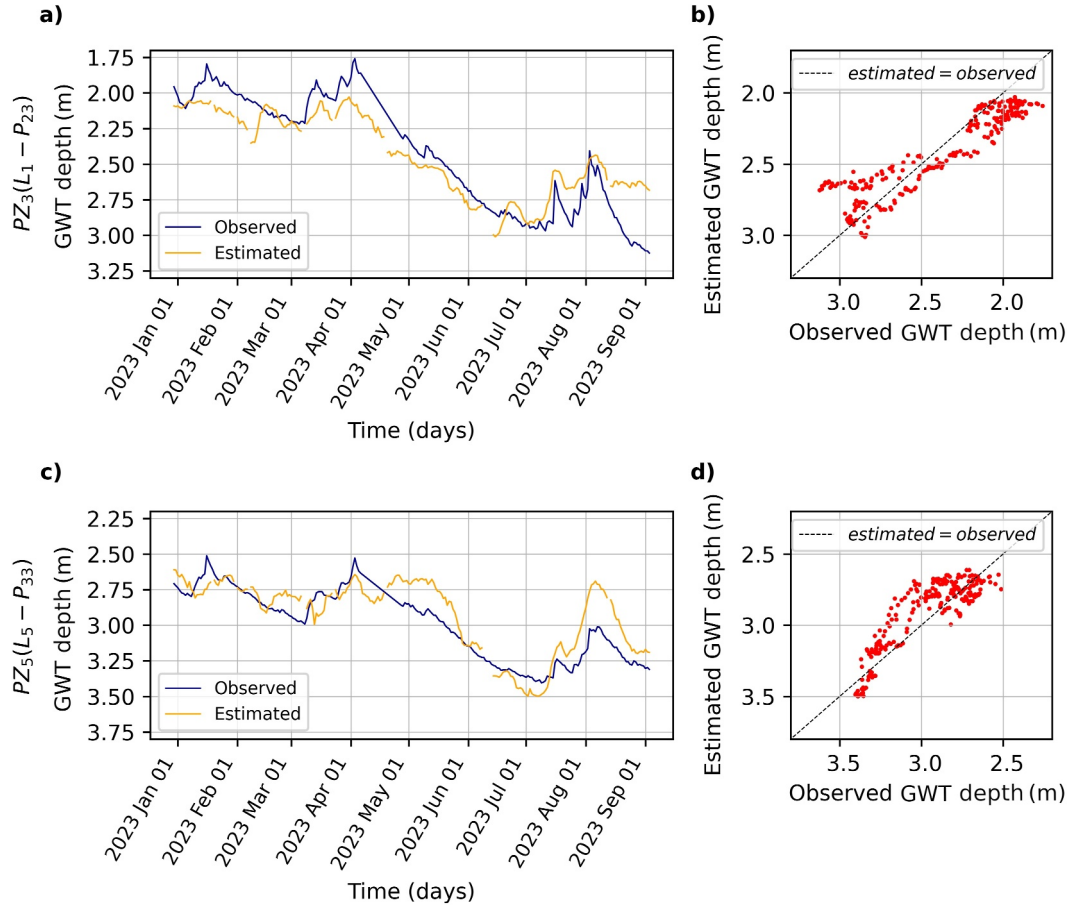

Figure 6. MLP's GWT depth estimations, obtained using DCs at seismic array points around PZ_3 (L_1-P_{22}, L_1-P_{23}, L_1-P_{24}, L_2-P_{21}, L_2-P_{22}, and L_2-P_{23}) and observed GWT depths at PZ_3 as training data. (a) GWT depth over time observed at PZ_3 and estimated at seismic array point L_1-P_{23}. (b) GWT depths observed at PZ_3 versus estimated at L_1-P_{23}. (c) GWT depth over time observed at PZ_5 and estimated at seismic array point L_5-P_{33}. (d) GWT depths observed at PZ_5 versus estimated at point L_5-P_{33}.

shallow depths at around 2 m, with minimal variation over time. Even more, we observe an inferred GWT that increased between the low and high water periods (around DR_1 and at the end of L_5 on Figures 7 and 8). These artifacts and non expected GWT depth variations could be explained by lower quality on the input DC data. In fact, it seems that mode contamination occurred during the picking process at certain position, where a higher mode was mistakenly picked between 30 and 50 Hz (see $L_5 - P_{39}$ to $L_5 - P_{43}$ on Figure A7). Additionally, the area enclosed from $L_5 - P_1$ to $L_5 - P_5$ also shows poor quality, with DCs around April appearing to be underestimated (see Figure A7).

As expected, the model appears to be sensitive to the quality of the input data, highlighting the critical importance of the DC processing and quality control in accurately inferring GWT depths. Such issues (O'Neill & Matsuoka, 2005) cannot be yet perfectly addressed in an automatic processing workflow. However, the current study, which has to be seen as a proof of concept, remains very encouraging and should provide better results as soon as the automatic data processing workflow is improved.

Additionally, to assess the influence of the number of piezometers on the estimated GWT maps, a model was trained using data points around PZ_3 (L_1-P_{22}, L_1-P_{23}, L_1-P_{24}, L_2-P_{21}, L_2-P_{22} and L_2-P_{23}) and PZ_5 (L_4-P_{31}, L_4-P_{32}, L_4-P_{33}, L_5-P_{32}, L_5-P_{33} and L_5-P_{34}). The results, presented in Appendix B (see Figures B1–B5), reveal an enhanced estimation performance at both PZ_3 (R^2 of 88% and an RMSE of 0.01 m) and PZ_5 (R^2 of 72% and an RMSE of 0.01 m). Upon comparing the estimated GWT maps in Figure 7 (MLP trained with only PZ_3) and Figure B2 (MLP trained with both PZ_3 and PZ_5), it is evident that extreme high and low GWT depths appear to have been smoothed or flattened. Nevertheless, the general GWT depths and behavior remain highly consistent with the previous

10.1029/2024WR037706

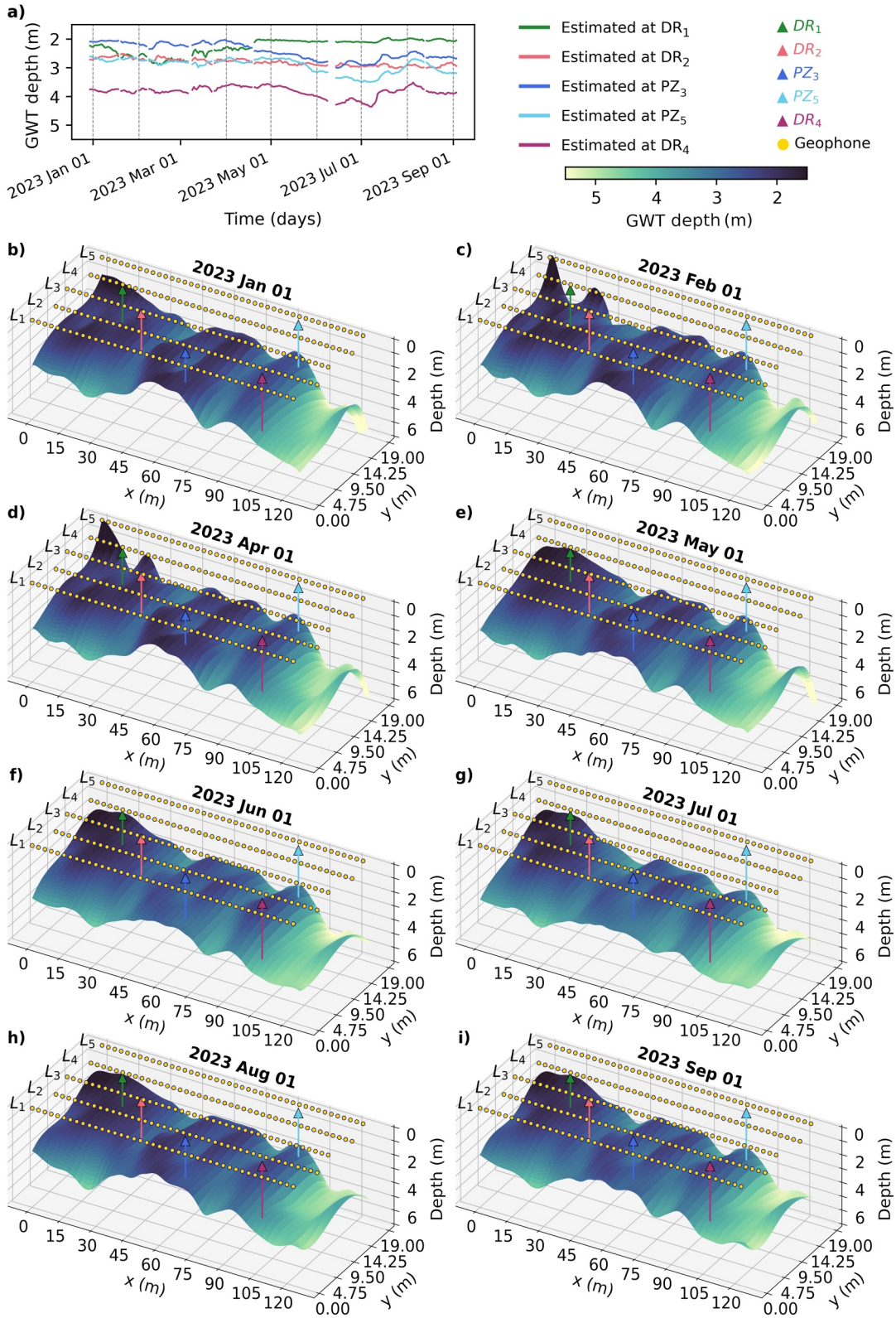

Figure 7. MLP's GWT depth estimations, obtained using DCs at seismic array points around PZ_3 (L_1-P_{22}, L_1-P_{23}, L_1-P_{24}, L_2-P_{21}, L_2-P_{22}, and L_2-P_{23}) and observed GWT depths at PZ_3 as training data. (a) Estimated GWT depths over time at the five drilling and piezometers locations. (b–i) Estimated GWT maps at different dates, with geophone linear array (L), piezometer (PZ) and drilling (DR) positions at the surface.

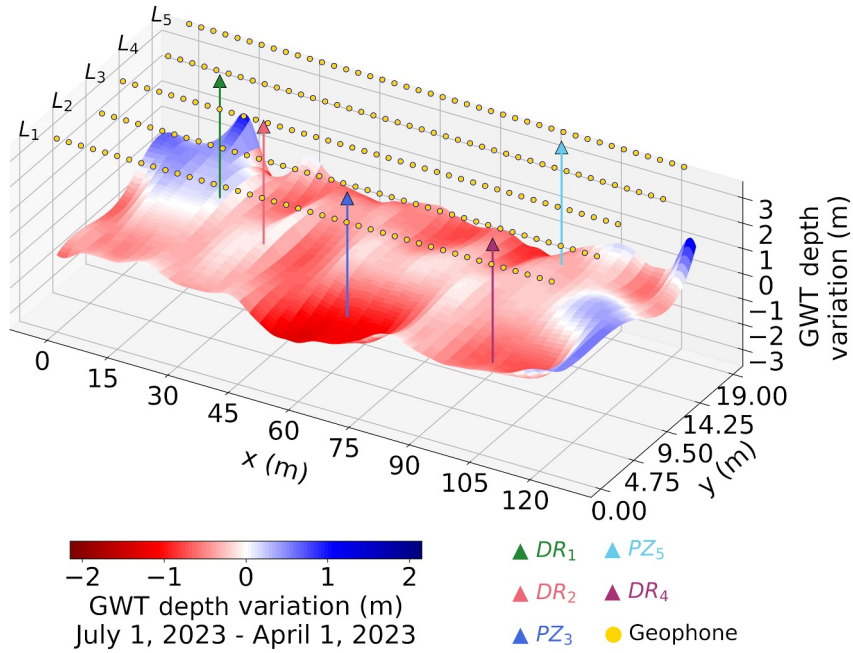

Figure 8. Estimated GWT depth map variation between high water period (1 April 2023) and low water period (1 July 2023), obtained using DCs at seismic array points around PZ_3 (L_1-P_{22}, L_1-P_{23}, L_1-P_{24}, L_2-P_{21}, L_2-P_{22}, and L_2-P_{23}) and observed GWT depths at PZ_3 as training data. Geophone, piezometer and drilling positions are displayed at surface.

estimations. This supports the robustness of using an unique piezometer for training. However, employing multiple piezometers, installed in different lithologies, enhances the precision and stability of the method.

It is also important to note that this study only included 9 months of GWT data, which is relatively limited and does not cover a full annual cycle. Monitoring over an entire year would provide a more comprehensive

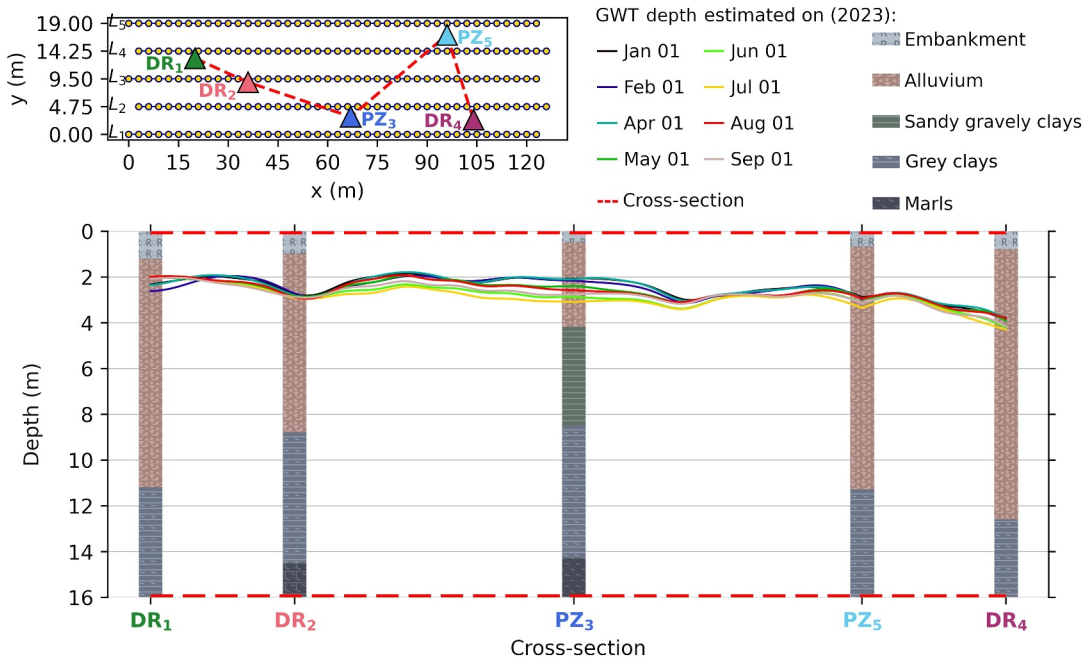

Figure 9.. (top) Geophone array map and cross-section line (in red) between drilling and piezometers. (bottom) Cross-section of estimated GWT depths at different dates, obtained using DCs at seismic array points around PZ_3 (L_1-P_{22}, L_1-P_{23}, L_1-P_{24}, L_2-P_{21}, L_2-P_{22}, and L_2-P_{23}) and observed GWT depths at PZ_3 as training data, with geologic logs illustrating the nature of the underground materials.

10.1029/2024WR037706

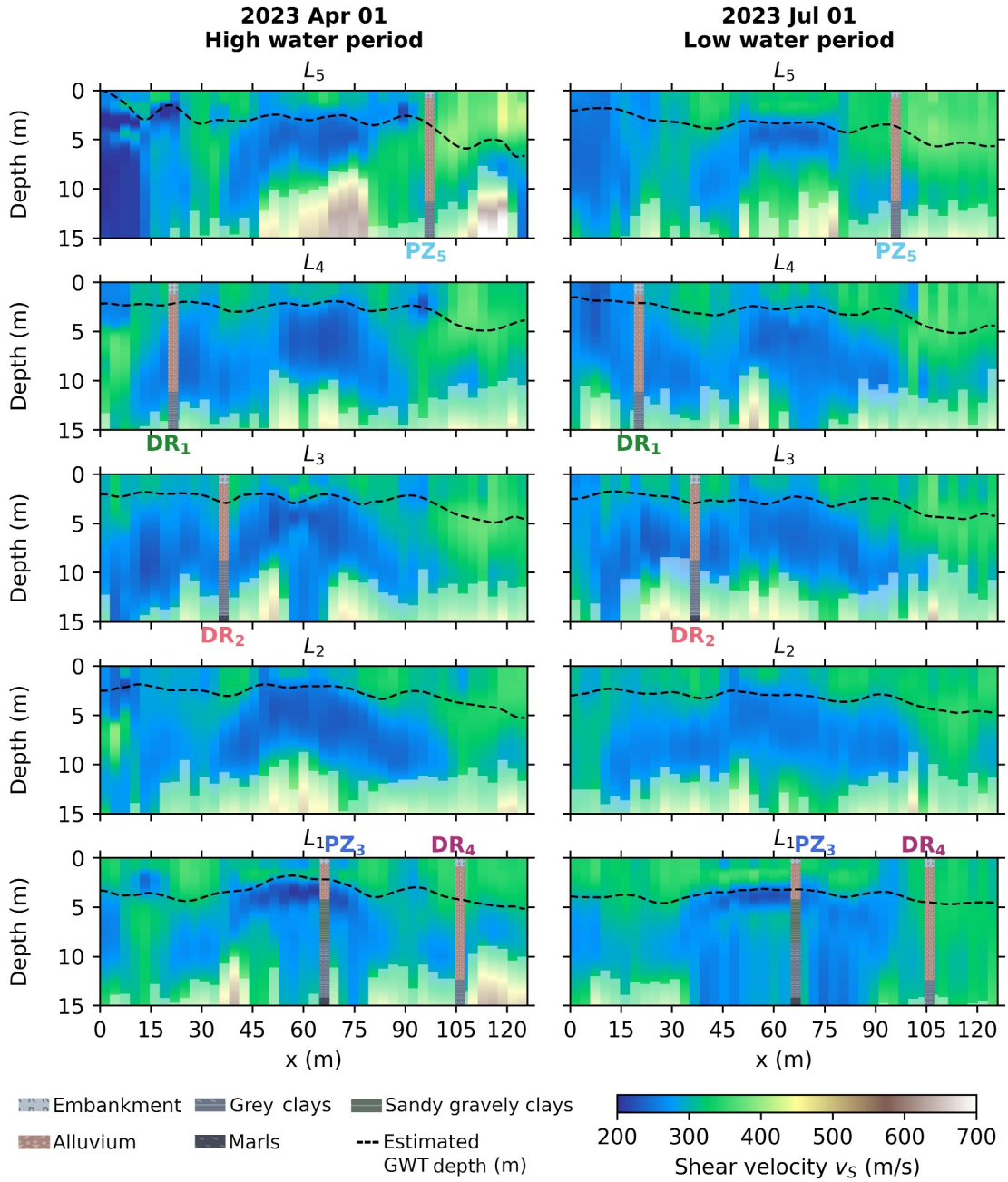

Figure 10. Inverted V_S sections over depth for the 5 linear geophone arrays (L_1 to L_5) at a high water period (1 April 2023) and at a low water period (1 July 2023). The white mask indicates depths where the standard deviation, between the mean V_S model and all other accepted models during inversion, is greater than 400 m/s. Estimated GWT depths, obtained using DCs at seismic array points around PZ_3 (L_1-P_{22}, L_1-P_{23}, L_1-P_{24}, L_2-P_{21}, L_2-P_{22}, and L_2-P_{23}) and observed GWT depths at PZ_3 as training data, and geologic logs, illustrating the nature of the underground materials at five drilling coordinates, are superposed for interpretation.

understanding of seasonal variations in GWT depths, capturing the full range of hydrological conditions. To further validate the model's accuracy and robustness, it would be beneficial to extend the study period to at least two annual cycles. This would allow for the inclusion of a full cycle from both piezometers in the training process, with the other cycle serving as the test data set for both piezometers.

While our current model is a relatively simple MLP with only two layers, we acknowledge that its ability to reproduce precise temporal dynamics of the GWT is limited. This limitation can be attributed to the sensitivity of the passive-MASW method, as it may not be sensitive enough to detect subtle daily variations in the GWT.

Additionally, it could also be the consequence of training the MLP using time-independent data. In fact, this study focused on approximating the inversion function linking a DC with a GWT depth, without incorporating temporal aspects. Consequently, the model does not explicitly learn the temporal dependencies between time consecutive GWT depths, making it challenging to capture time-series relationships effectively. To address this limitation, Recurrent Neural Networks (RNNs), particularly Long Short-Term Memory (LSTM) and Gated Recurrent Unit (GRU) architectures, could replace our MLP. These architectures are specifically designed to handle sequential numerical data and can learn temporal dependencies by retaining information from previous time steps when making predictions. However, this approach could limit the model's ability to extrapolate outside the training data set, as the GWT temporal behavior at the training location and at different array locations may not be identical. Additionally, the model would be highly sensitive to data consistency, as missing data could compromise the model's performance, and larger gaps in the data set would reduce the effectiveness of training. Adding rain data to the inputs could also help capturing the time dynamic of the GWT. However, the small scale of our study site limits us to a single data set for the entire array.

5.4. Future Applicability Directions

Our method benefits from the high spatial resolution provided by a dense array. However, it may also be applicable to sparser arrays, though with potentially reduced accuracy. The length of the geophone lines, and distance between geophones affect the maximum measurable wavelength in the DCs (L. Socco & Strobbia, 2004). Therefore, it is essential to ensure that the GWT depth is sensitive to the wavelengths captured by the signal (see Section 2.2). In sparser arrays, the captured wavelengths might not fully encompass the shallow GWT. However, for deeper aquifers, a sparser array on a regional scale might be appropriate, as it would allow for the capture of longer wavelengths that are sensitive to deeper structures. While this approach may result in lower spatial resolution, it could still effectively characterize broader valuable insights into GW dynamics at larger scales.

While our study primarily focused on seismic signals generated by passing trains, the method is not limited to this specific source. It could also be adapted for use with other ambient noise sources, or even periodic active sources like controlled mechanical vibrations. The critical requirement is that the chosen signals must generate detectable surface waves and be recorded consistently enough to allow for reliable time analysis. Ambient noise, for instance, is a ubiquitous and continuous source, making it a good candidate for long-term monitoring applications. However, an active source can generate higher frequencies compared to ambient noise, which is particularly useful for characterizing shallow GWTs with high resolution.

Our study serves as a proof of concept for the capability of DL to approximate a complex function between depth-sensitive geophysical data and GWT depths. In fact, we believe that other types of geophysical data could potentially replace DCs in the workflow. For example, electrical resistivity tomography (ERT), V_S seismic tomography, Love-wave dispersion analysis, and other depth-sensitive geophysical methods could be used, or even combined (when it is possible considering the very constraining railway context, as specified by Burzawa et al. (2023) for instance). Multi-modal DCs could also significantly improve the model's ability to constrain the depth of the GWT.

6. Conclusions

This study introduces a physics-guided DL model combining 2D passive-MASW with an MLP to estimate daily GWT maps from a single piezometer, and offering an effective mean of monitoring GWTs with both spatial and temporal precision. This hybrid approach exhibited notable generalization capabilities, with the ability to spatially extrapolate GWT maps beyond the training piezometric data set. Analysis of GWT maps revealed spatial and temporal variations, offering a nuanced understanding of GWT geometry and dynamics, and revealing valuable hydrogeological insights. The model successfully captured variations associated with lithological changes, demonstrating its efficacy in characterizing subsurface materials. In addition, the estimated GWT depths align closely with low-velocity layers, in terms of V_S, indicative of saturated alluvium and shallow clay layers. However, while the study demonstrates promising results, it is crucial to acknowledge its limitations. The model's performance may be influenced by site-specific conditions, and further validation across diverse geological settings is needed. By leveraging geophysical data and DL, this study contributes to advancing our understanding of subsurface dynamics and offers practical insights for effective GW management and risk mitigation strategies.

This integrated approach can be applied to monitor aquifer resilience at different scales, contribute to informed decision-making in the context of water resource management, and assess potential hazards such as sinkholes.

Appendix A: Raw Data

Figure A1 shows the same V_R pseudo-sections presented in Figure 2, at a high water period on 1 April 2023, and at a low water period on 1 July 2023, but with the original DCs sampled over frequencies ranging from 5 to 50 Hz. Figure A2 illustrates the non-linear relationship between GWT depths and Rayleigh-wave phase velocities at

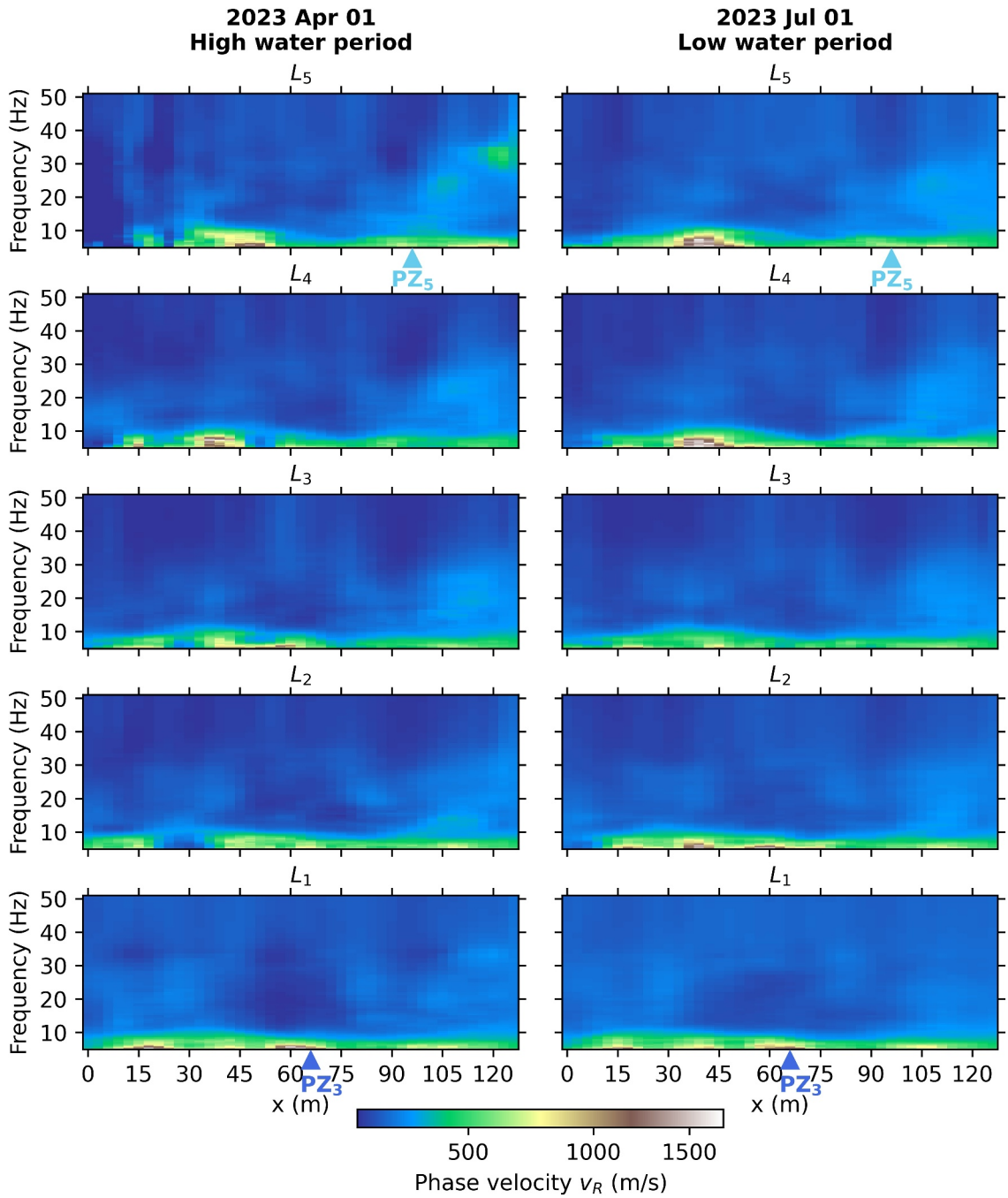

Figure A1. V_R pseudo-sections over frequencies for the 5 linear geophone arrays (L_1 to L_5) (left) at a high water period on 1 April 2023, and (right) at a low water period on 1 July 2023. Positions of piezometers PZ_3 and PZ_5 are represented by the blue triangles on profiles L_1 and L_5, respectively.

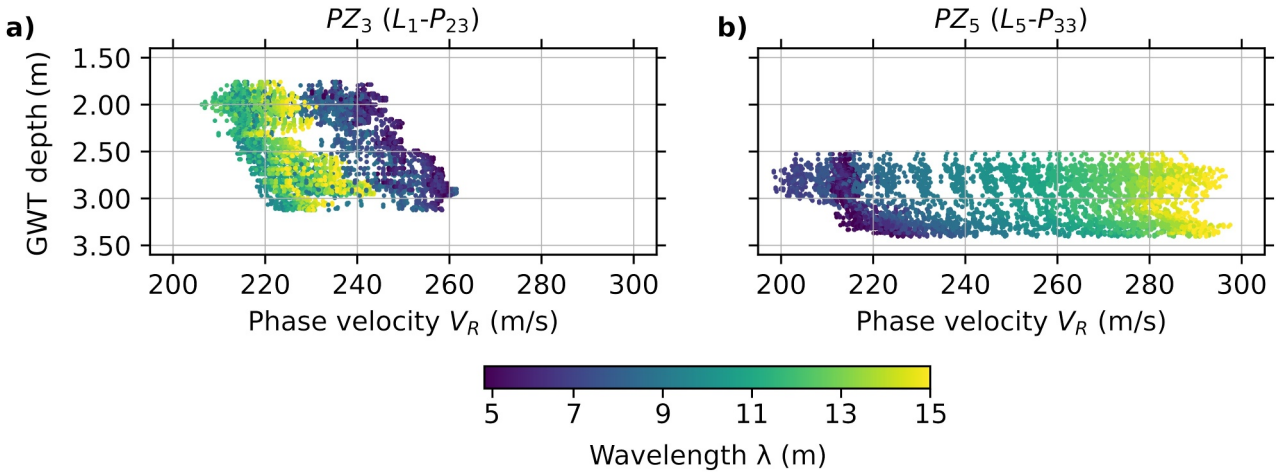

Figure A2. GWT depths in function of the Rayleigh-wave phase velocity V_R, for different wavelengths (represented by the colorbar), at both piezometers PZ_3 and PZ_5, between 30 December 2022, and 3 September 2023.

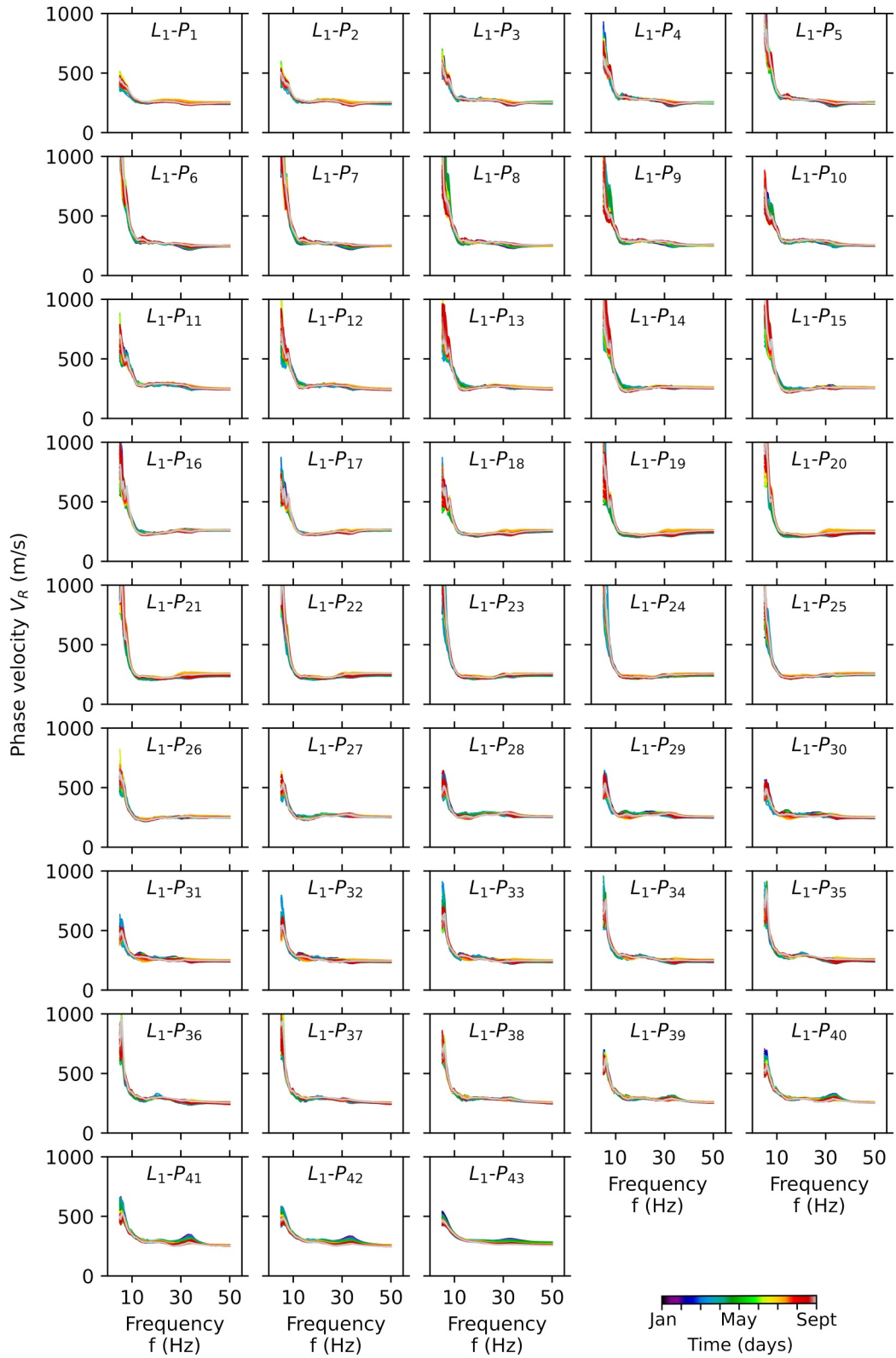

Figure A3. Dispersion curves along the geophone line L_1, between 30 December 2022, and 3 September 2023.

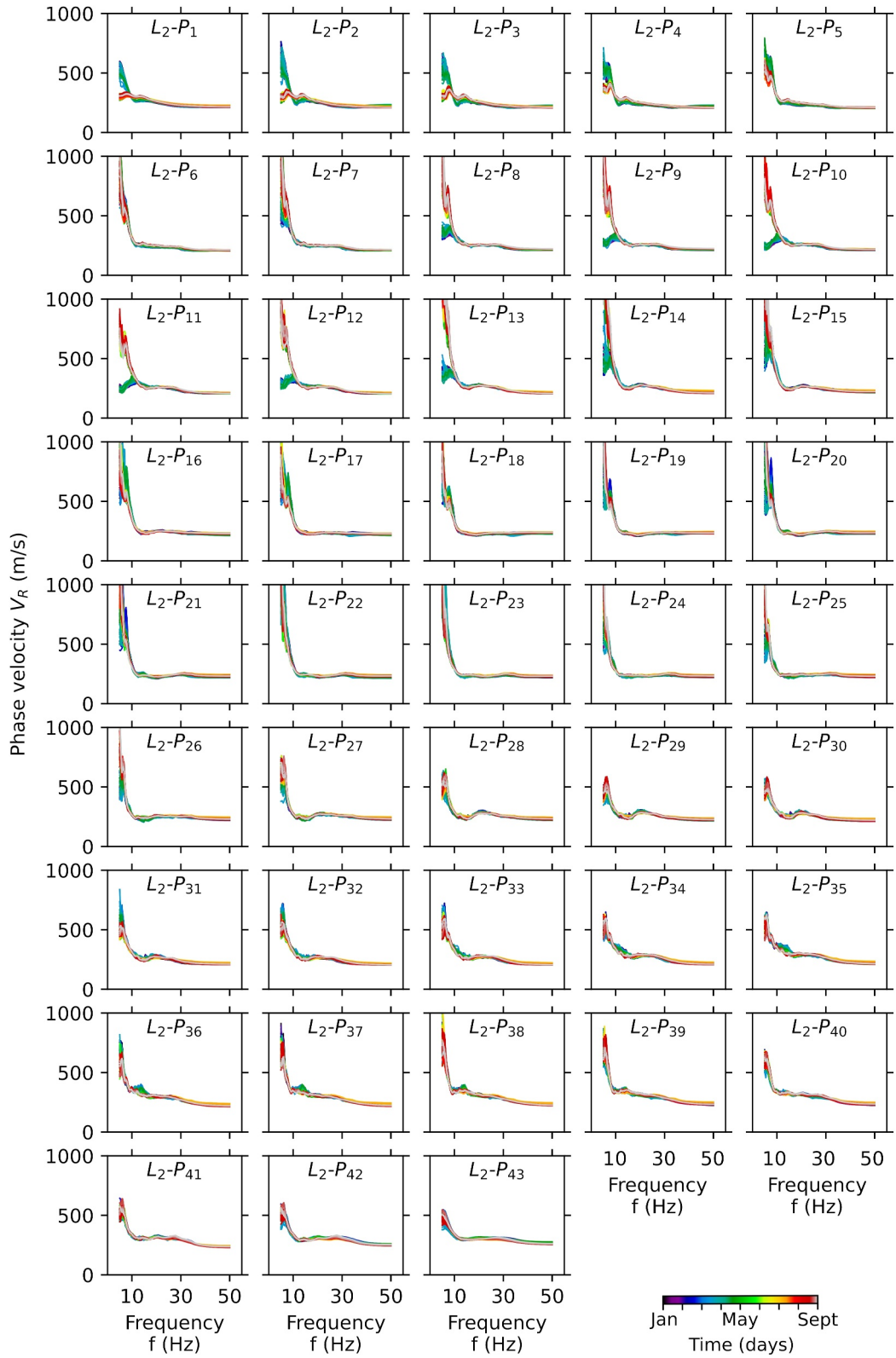

Figure A4. Dispersion curves along the geophone line L_2, between 30 December 2022, and 3 September 2023.

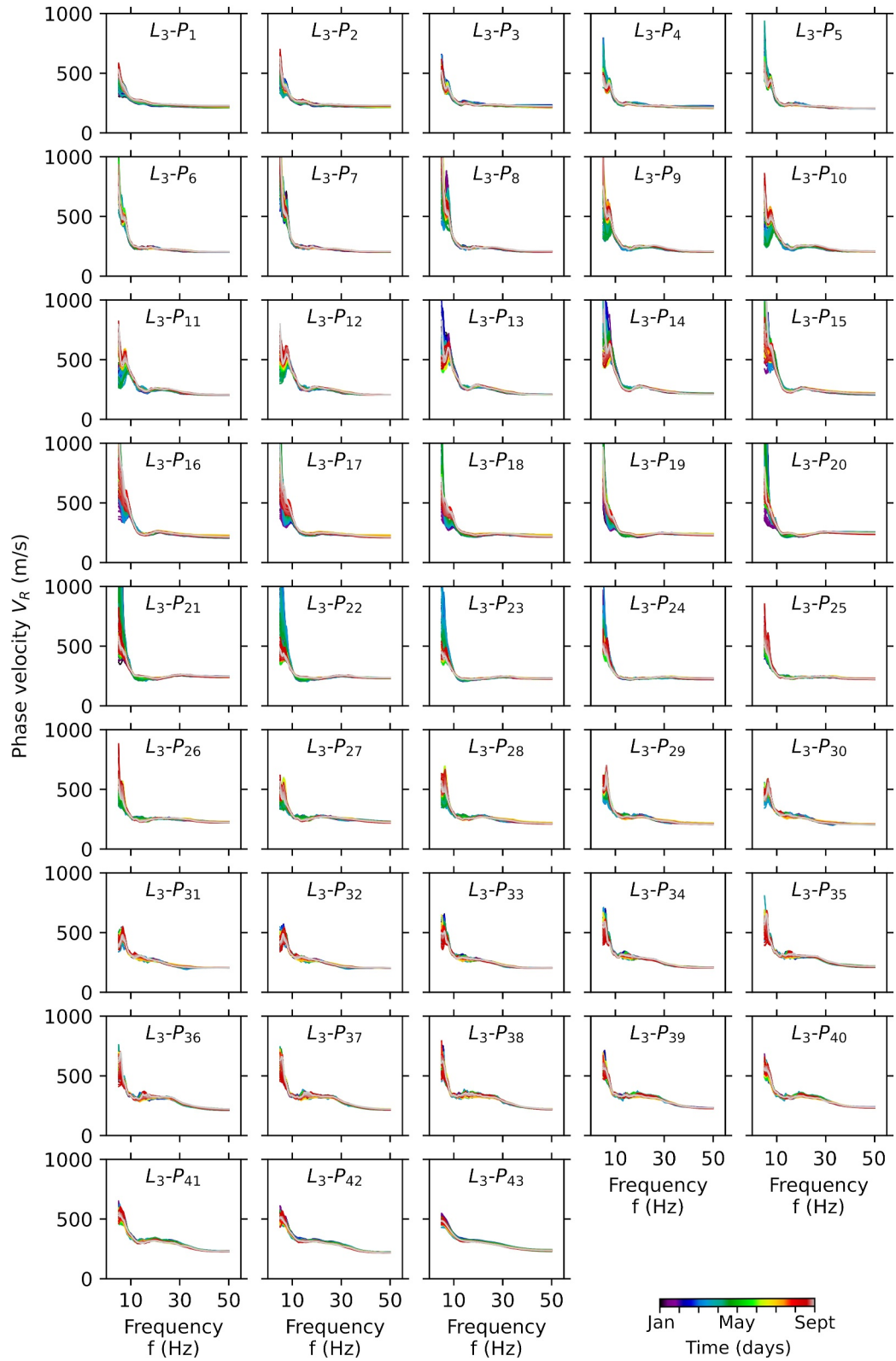

Figure A5. Dispersion curves along the geophone line L_3, between 30 December 2022, and 3 September 2023.

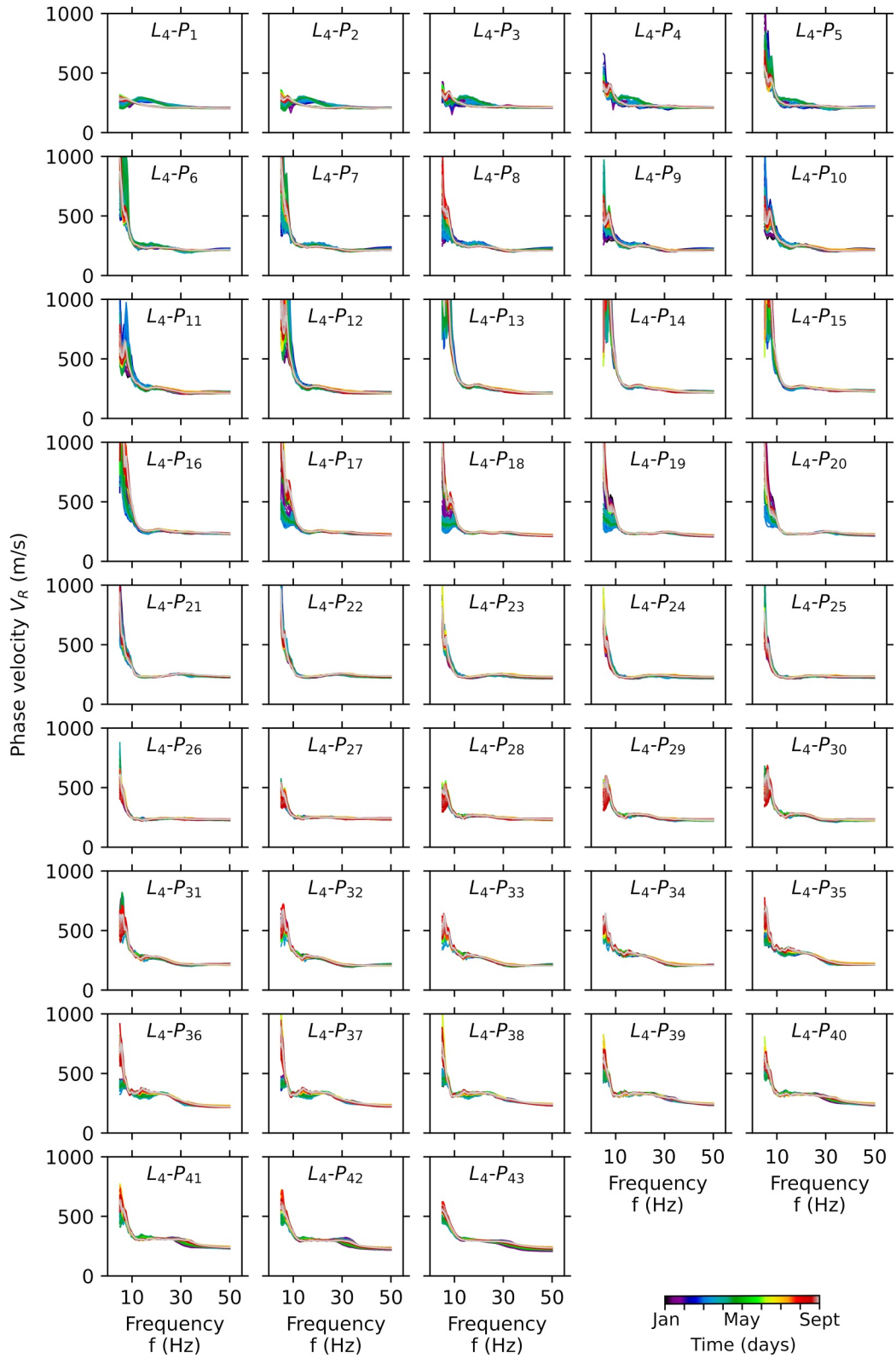

Figure A6. Dispersion curves along the geophone line L_4, between 30 December 2022, and 3 September 2023.

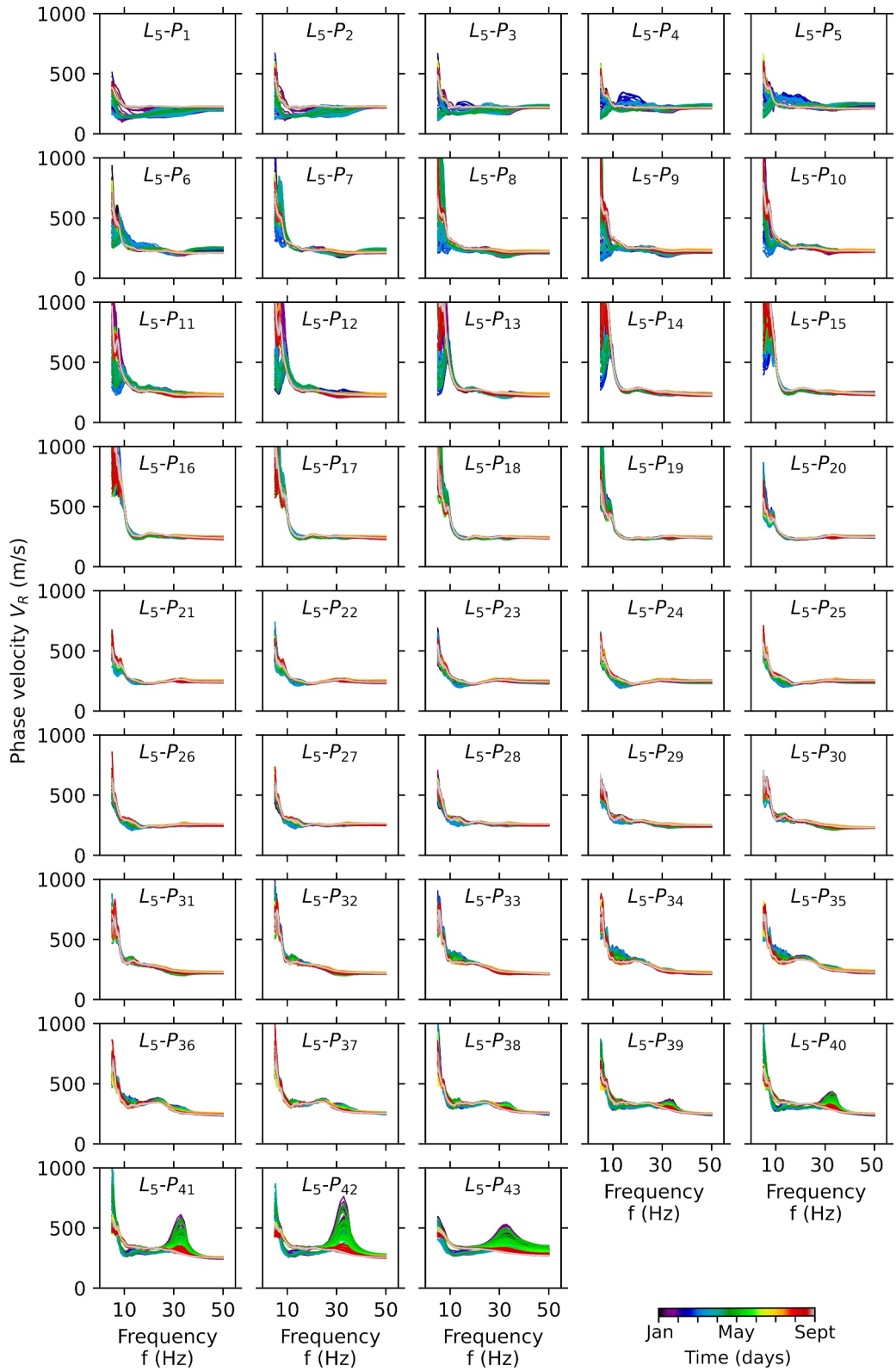

Figure A7. Dispersion curves along the geophone line L_5, between 30 December 2022, and 3 September 2023.

various wavelengths. Finally, Figures A3–A7 show the raw DCs along each geophone line, between 30 December 2022 and 3 September 2023.

Appendix B: Model Trained With Both Piezometers

In this section, we present the same study, but incorporating results from an MLP model trained using seismic and GWT depth data from both piezometers. The expanded data set enhances the model's training with a more comprehensive understanding of the subsurface dynamics at multiple locations. By integrating seismic and GWT data from both piezometers, we aim to provide a more robust and nuanced analysis of the GWT variations and their correlation with the subsurface characteristics. Results are similar to those obtained using a single piezometer for training, and are discussed in Section 5.

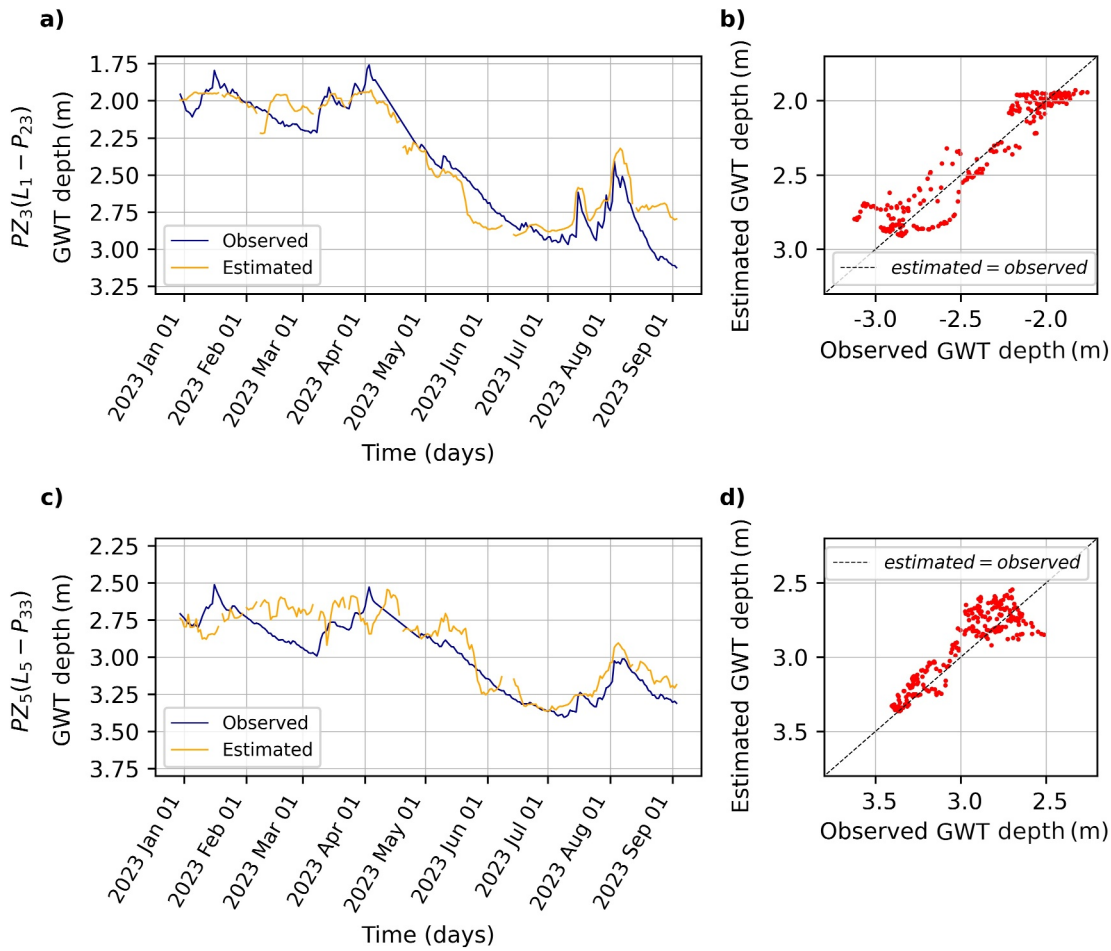

Figure B1. MLP's GWT depth estimations, obtained using DCs at seismic array points around PZ_3 (L_1-P_{22}, L_1-P_{23}, L_1-P_{24}, L_2-P_{21}, L_2-P_{22}, and L_2-P_{23}) and PZ_5 (L_4-P_{31}, L_4-P_{32}, L_4-P_{33}, L_5-P_{32}, L_5-P_{33}, and L_5-P_{34}), and observed GWT depths at PZ_3 and PZ_5 as training data. (a) GWT depth over time observed at PZ_3 and estimated at seismic array point L_1-P_{23}. (b) GWT depths observed at PZ_3 versus estimated at L_1-P_{23}. (c) GWT depth over time observed at PZ_5 and estimated at seismic array point L_5-P_{33}. (d) GWT depths observed at PZ_5 versus estimated at point L_5-P_{33}.

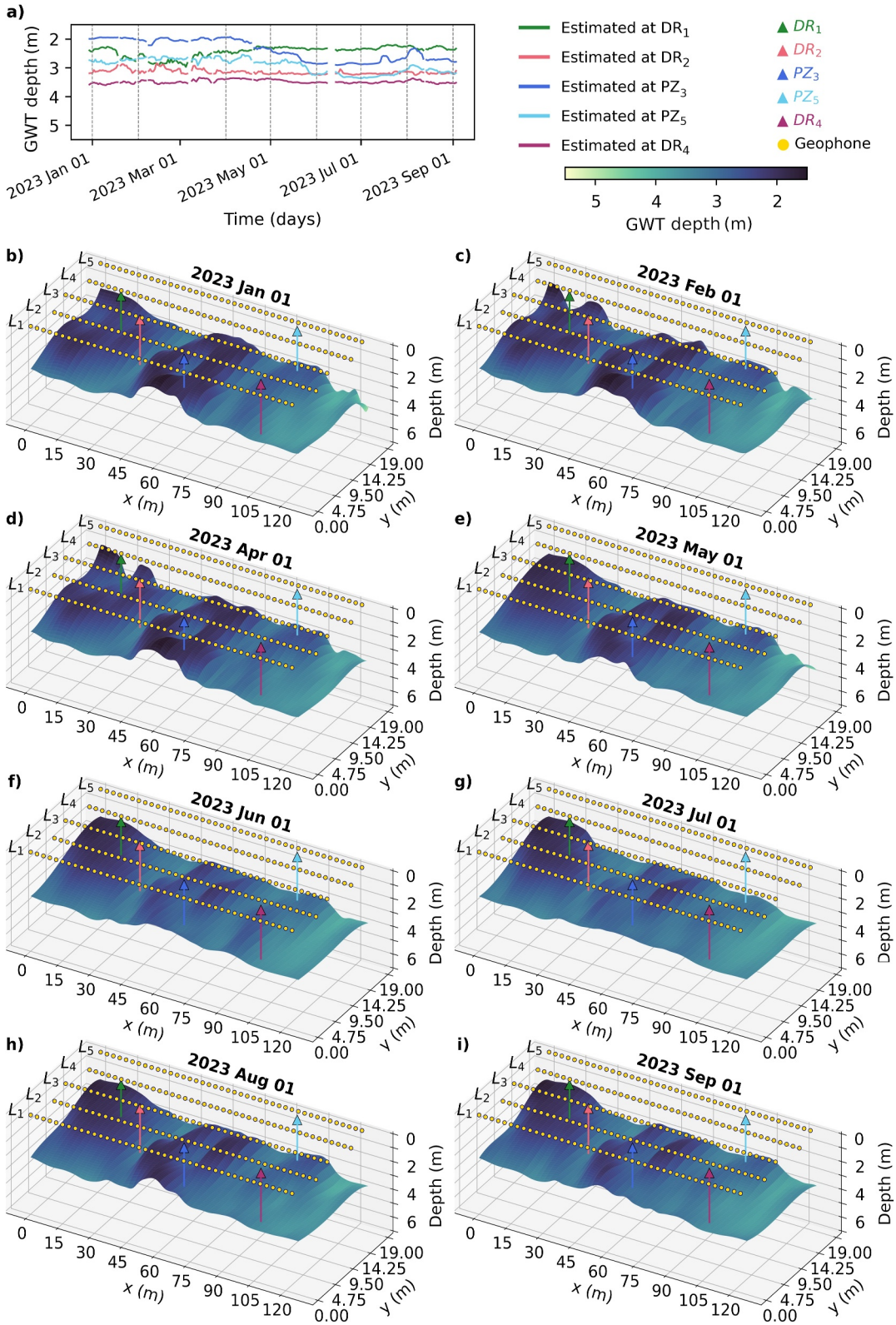

Figure B2. MLP's GWT depth estimations, obtained using DCs at seismic array points around PZ_3 (L_1-P_{22}, L_1-P_{23}, L_1-P_{24}, L_2-P_{21}, L_2-P_{22}, and L_2-P_{23}) and PZ_5 (L_4-P_{31}, L_4-P_{32}, L_4-P_{33}, L_5-P_{32}, L_5-P_{33}, and L_5-P_{34}), and observed GWT depths at PZ_3 and PZ_5 as training data. (a) Estimated GWT depths over time at the five drilling and piezometers locations. (b–i) Estimated GWT maps at different dates, with geophone linear array (L), piezometer (PZ) and drilling (DR) positions at the surface.

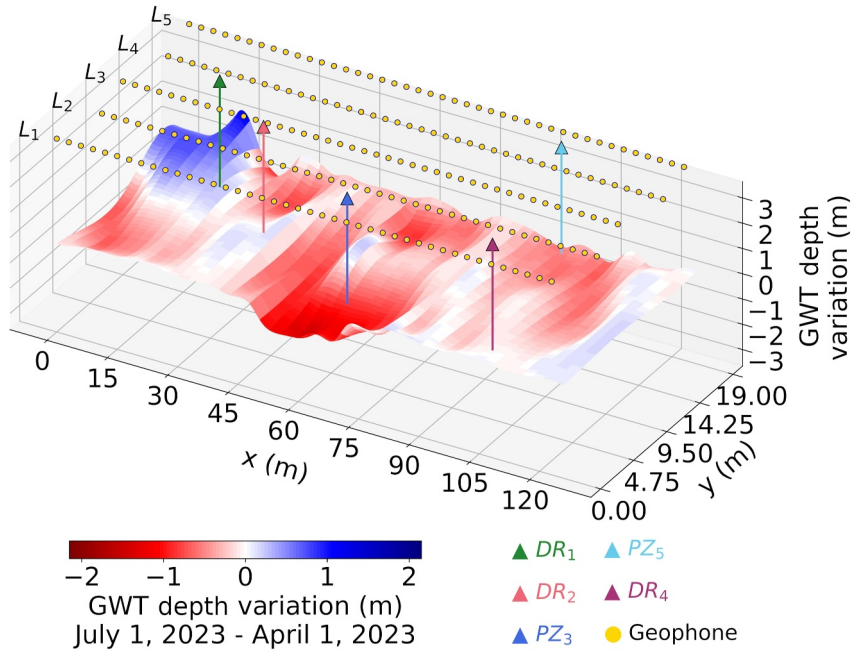

Figure B3. Estimated GWT map variation between high water period (1 April 2023) and low water period (1 July 2023), obtained using DCs at seismic array points around PZ_3 (L_1-P_{22}, L_1-P_{23}, L_1-P_{24}, L_2-P_{21}, L_2-P_{22}, and L_2-P_{23}) and PZ_5 (L_4-P_{31}, L_4-P_{32}, L_4-P_{33}, L_5-P_{32}, L_5-P_{33}, and L_5-P_{34}), and observed GWT depths at PZ_3 and PZ_5 as training data. Geophone, piezometer and drilling positions are displayed at surface.

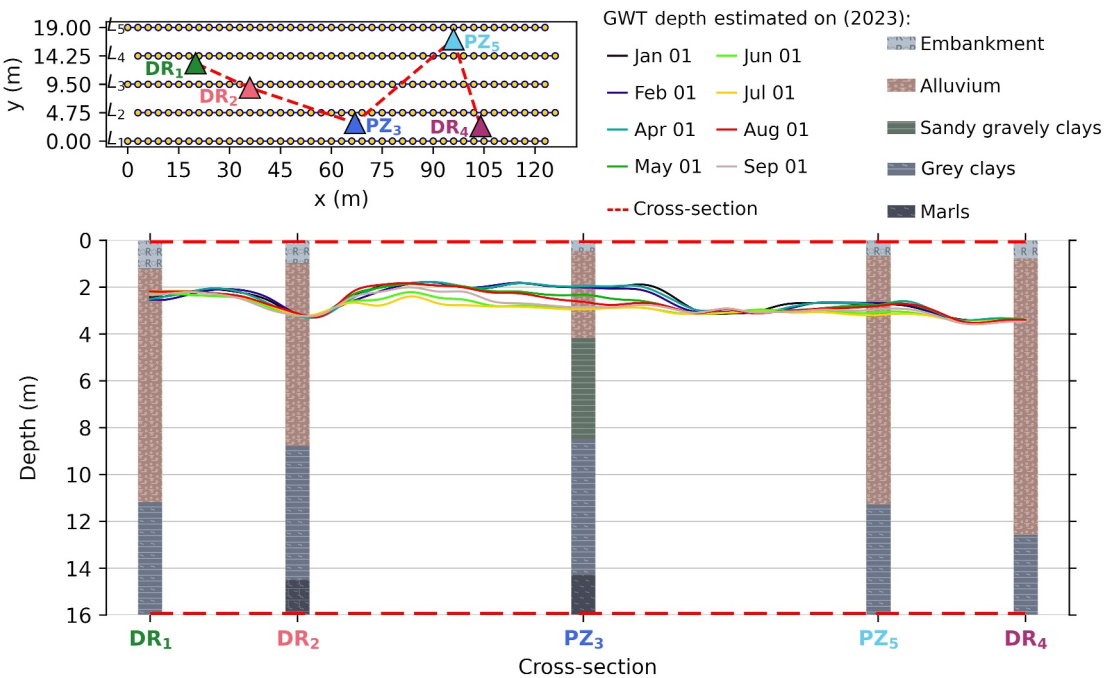

Figure B4. (top) Geophone array map and cross-section line (in red) between drilling and piezometers. (bottom) Cross-section of estimated GWT depths at different dates, obtained using DCs at seismic array points around PZ_3 (L_1-P_{22}, L_1-P_{23}, L_1-P_{24}, L_2-P_{21}, L_2-P_{22}, and L_2-P_{23}) and PZ_5 (L_4-P_{31}, L_4-P_{32}, L_4-P_{33}, L_5-L_5-P_{33}, and L_5-P_{34}), and observed GWT depths at PZ_3 and PZ_5 as training data, with geologic logs illustrating the nature of the underground materials.

10.1029/2024WR037706

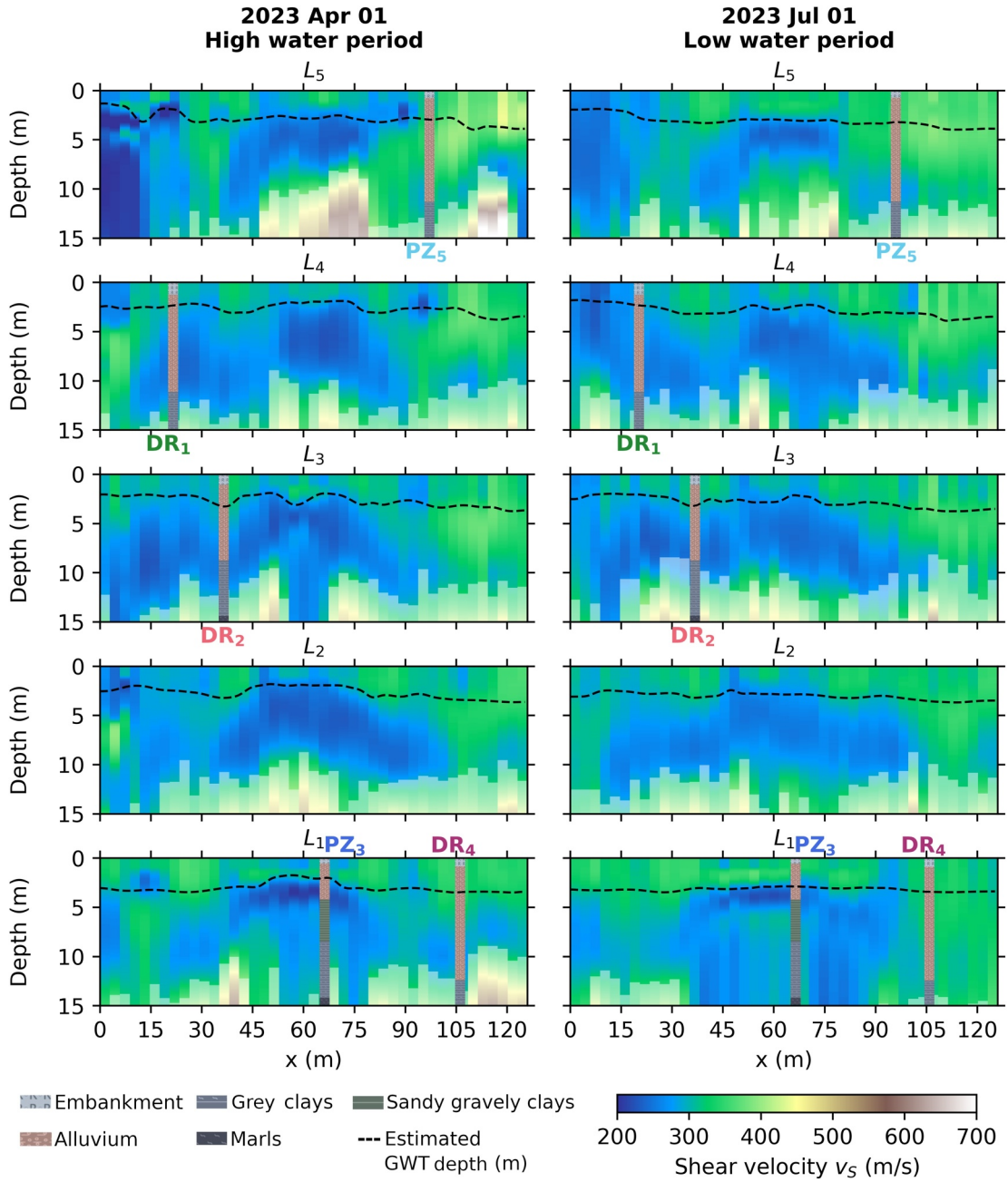

Figure B5. Inverted V_S sections over depth for the 5 linear geophone arrays (L_1 to L_5) at a high water period (1 April 2023) and at a low water period (1 July 2023). The white mask indicates depths where the standard deviation, between the mean V_S model and all other accepted models during inversion, is greater than 400 m/s. Estimated GWT depths, obtained using DCs at seismic array points around PZ_3 (L_1-P_{22}, L_1-P_{23}, L_1-P_{24}, L_2-P_{21}, L_2-P_{22}, and L_2-P_{23}) and PZ_5 (L_4-P_{31}, L_4-P_{32}, L_4-P_{33}, L_5- and L_5-P_{34}), and observed GWT depths at PZ_3 and PZ_5 as training data., and geologic logs, illustrating the nature of the underground materials at five drilling coordinates, are superposed for interpretation.

Appendix C: Inversion

For each seismic linear array, V_R over frequencies pseudo-sections, corresponding to DCs along x (fundamental mode M_0), obtained by passive-MASW, were inverted to generate a V_S over depth sections. We use the open-source software package SWIP (https://github.com/spasquet/SWIP) implemented by Pasquet and Bodet (2017), that is built upon the software Dinver (https://www.geopsy.org/wiki/index.php/Dinver:_dinverdc) using a *neighborhood algorithm* developed by Sambridge (1999) and implemented by Wathelet (2008), to solve

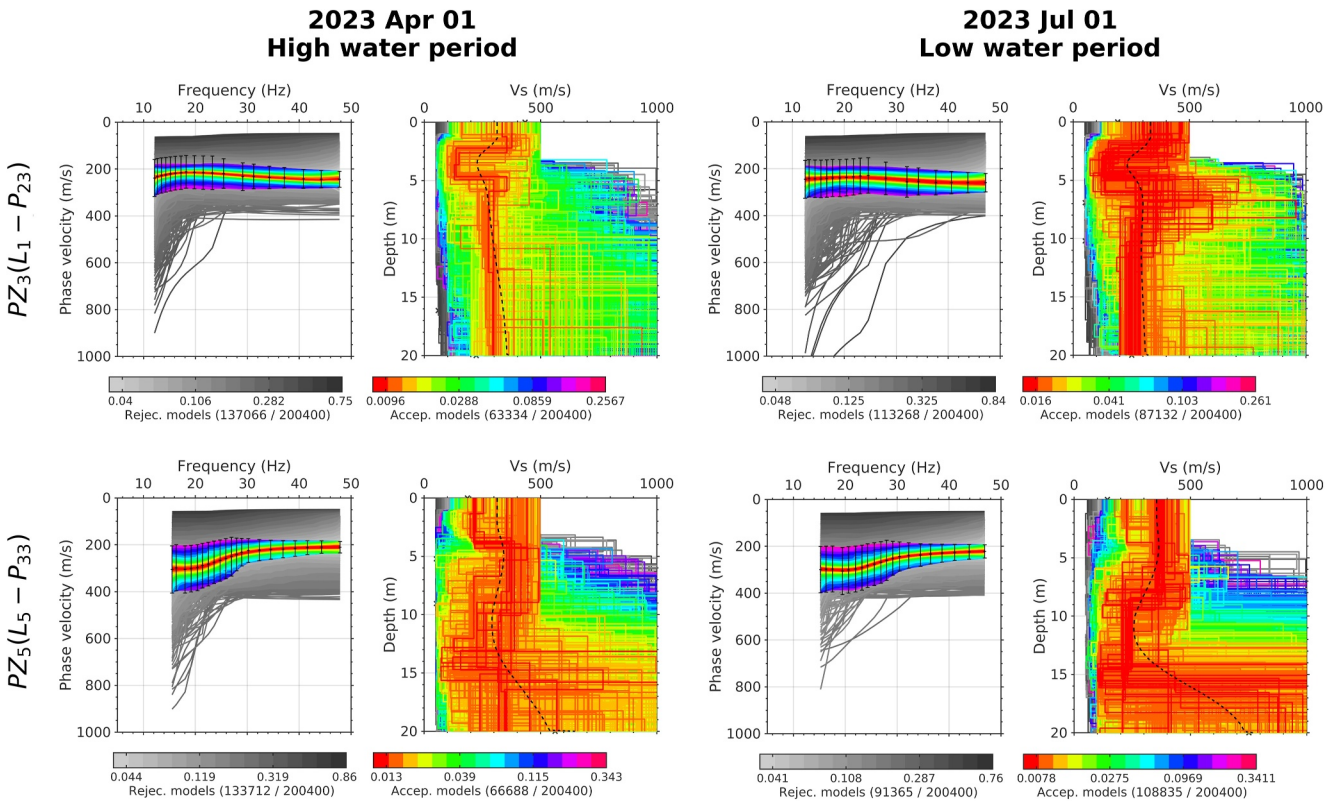

Figure C1. Inversion results at seismic array points (top) L_1-P_{23}, close to *PZ*3, and (bottom) L_5-P_{33}, close to *PZ*5, on (left) on 1 April 2023, and 1 July 2023. (a, c, e, and g) shows the modeled DCs, with error-bars, for the fundamental mode. (b, d, f, and h) represent the modeled velocity models. Each DC and velocity model is represented with a color depending on the misfit value between the modeled and experimental DCs (black crosses and error-bars). The models inside the error-bars, in terms of DCs, are plotted in color, and the rest are plotted in a gray scale. Plotted from the inversion software SWIP.

the inverse problem in a juxtaposed 1D setup. The inversion was parameterized with five layers, including an half-space, in accordance with the drilling data (see PZ_3 in Figure 1). This method involves a stochastic exploration of a parameter space in order to search for a minimum misfit between measured and simulated DCs. The chosen parameter space, as outlined in Table C1, encompasses various key parameters including layer thicknesses, pressure-wave velocity (V_P), shear-wave velocity (V_S), density (ρ), and Poisson's ratio (ν). The deliberate selection of a large parameter space stems from the limited a priori information about the mechanical properties of the geological layers. This approach ensures that the inversion process remains explorative, unbiased, and is capable of capturing a wide range of geological scenarios that may influence the seismic response in the study area. For each DC along the seismic linear arrays, out of a total 200,400 simulated models, only the models with DCs within the error-bars are accepted and averaged to generate final average smooth velocity models. The DCs' uncertainty $\delta_c(f)$ represented by error-bars was calculated in accordance with Pasquet and Bodet (2017):

Table C1
Inversion Parameter Space

Layer ()	Thickness (m)	V_P(m/s)	V_S(m/s)	ρ(kg/m^3)	ν
1	1–10	100–1,000	50–500	2,000–2,500	0.1–0.5
2	1–10	100–1,000	50–500	2,000–2,500	0.1–0.5
3	1–10	100–1,000	50–500	2,000–2,500	0.1–0.5
4	1–20	200–2,000	100–1,000	2,000–2,500	0.1–0.5
½-space	∞	400–4,000	200–2,000	2,000–2,500	0.1–0.5

Note. V_P, P-wave velocity; V_S, S-wave velocity; ρ, density; ν, Poisson's ratio.

Table C2
Inversion Running Parameters in SWIP

Parameter	Value	Description
n_{run}	4	Number of runs
$it_{\max}$	250	Number of iterations per run
ns_0	100	Number of starting models
ns	200	Number of modes created at each iteration
nr	100	Number of previous models to build new sub-parameter space

$$\delta_c(f) = 10^{-a}\left|\frac{1}{\frac{1}{V_R(f)} - \frac{1}{2fN_x\Delta_x}} - \frac{1}{\frac{1}{V_R(f)} + \frac{1}{2fN_x\Delta_x}}\right|, \tag{C1}$$

with a being the logarithmic reduction factor, usually 0.5, N_x the number of geophones in the MASW window, and Δ_x the space interval between geophones.

As examples, we present the inversion results at PZ_3 and PZ_5 positions on 1 April 2023, and 1 July 2023. Figure C1 shows the velocity models and corresponding DCs simulated during the inversion on 1 April 2023, and 1 July 2023, respectively. The running parameters used in SWIP are outlined in Table C2. Each DC and velocity model is represented with a color depending on the misfit value (MF) between the experimental data (black crosses and error-bars) and the simulated dispersion defined as:

$$MF = \sqrt{\sum_{i=1}^{N_f} \frac{(V_{sim_i} - V_{\exp_i})^2}{N_f \sigma_i^2}}, \tag{C2}$$

with V_{sim_i} and $V_{\exp_i}$ being the simulated and experimental phase velocities at each frequency f_i, N_f the number of frequency samples, and σ_i the phase-velocity measurement uncertainty (error-bars) at each frequency f_i.

Appendix D: Error Computation

The *root mean squared error* (RMSE) corresponds to the expected value of the squared error or loss. If $\hat{y}_i$ is the predicted value of the i-th samples, and y_i is the corresponding true value, then the RMSE estimated over $n_{samples}$ is defined as:

$$RMSE(y, \hat{y}) = \sqrt{\frac{1}{n_{samples}} \sum_{i=1}^{n_{samples}} (y_i - \hat{y}_i)^2}. \tag{D1}$$

The coefficient of determination, usually denoted R^2, represents the proportion of variance that has been explained by the independent variables in the model. It provides an indication of goodness of fit and therefore a measure of how well unseen samples are likely to be predicted by the model, through the proportion of explained variance. If $\hat{y}_i$ is the predicted value of the i-th samples, and y_i is the corresponding true value, then the R^2 score over $n_{samples}$ is defined as:

$$R^2(y, \hat{y}) = 1 - \frac{\sum_{i=1}^{n_{samples}} (y_i - \hat{y}_i)^2}{\sum_{i=1}^{n_{samples}} (y_i - \tilde{y}_i)^2}, \tag{D2}$$

where $\tilde{y} = \frac{1}{n_{samples}} \sum_{i=1}^{n_{samples}} y_i$ is the arithmetic mean value of y.

Data Availability Statement

All authors approved the final version of this article. Input data files and software scripts used for the GWT depth estimations are publicly available in Cunha Teixeira (2024).

Acknowledgments
This research was made possible through funding from SNCF Réseau, CNRS, Sorbonne Université, Mines Paris-PSL research contract, and the ANRT/Cifre-SNCF Réseau No. 2021/1552 convention. It is essential to acknowledge the contribution of the team involved in acquiring and processing the geophysical passive-MASW data. In fact, the successful execution of this study owes much to the efforts of the Sercel Company, and particularly to the dedicated individuals Thomas Bardainne, Renaud Tarnus, Thibaut Allemand, Ceifang Cai, Helene Toubiana Lille, Nicolas Deladerriere, Lilas Vivin, and Loic Michel. The authors also express gratitude to the local teams from SNCF Réseau their invaluable assistance and support, notably to Sanae El Janyani for the hydrogeological study support, and Fabrice Pierron for the GIS cartography. The deep learning model was implemented using Python package Keras (Chollet, 2015). Dispersion curve inversions were conducted using the open-source software package SWIP (https://github.com/spasquet/SWIP), implemented by Pasquet and Bodet (2017).

References

Abi Nader, A., Albaric, J., Steinmann, M., Hibert, C., Malet, J.-P., Sue, C., et al. (2023). Machine learning prediction of groundwater heights from passive seismic wavefield. *Geophysical Journal International*, *234*(3), 1807–1818. https://doi.org/10.1093/gji/ggad160

Aki, K. (1957). Space and time spectra of stationary stochastic waves, with special reference to microtremors. *Bulletin of the Earthquake Research Institute*, *35*, 415–456.

Altunkaynak, A., & Strom, K. B. (2009). A predictive model for reach morphology classification in mountain streams using multilayer perceptron methods. *Water Resources Research*, *45*(12), W12501. https://doi.org/10.1029/2009WR008055

Barajas, A., Poli, P., D'Agostino, N., Margerin, L., & Campillo, M. (2021). Separation of poroelastic and elastic processes of an aquifer from tectonic phenomena using geodetic, seismic, and meteorological data in the Pollino region, Italy. *Geochemistry, Geophysics, Geosystems*, *22*(11), e2021GC009742. https://doi.org/10.1029/2021GC009742

Bardainne, T., Cai, C., Rebert, T., Tarnus, R., & Allemand, T. (2023). Passive seismic monitoring using trains as sources to characterize near-surface and prevent sinkholes. In *Passive seismic monitoring using trains as sources to characterize near-surface and prevent sinkholes* (Vol. 2023, p. 1–5). European Association of Geoscientists and Engineers. https://doi.org/10.3997/2214-4609.2023101262

Bardainne, T., & Rondeleux, B. (2018). Method and device for monitoring the subsoil of the earth under a target zone (patent No. FR3084473B1). Retrieved from https://patents.google.com/patent/WO2020021177A1/en?inventor=Bardainne&oq=Bardainne

Bardainne, T., Tarnus, R., Deladerriere, N., Hallier, A., Boisson-Gaboriau, J., Valentin, J., & Bouhdiche, O. (2022). Permanent passive seismic monitoring of the near-surface ground beneath railways using trains as sources. In *Fifth international conference on railway technology: Research, development and maintenance* (Vol. 1, p. 14). https://doi.org/10.4203/ccc.1.10.14

Bardainne, T., Tarnus, R., Vivin, L., Cai, C., Rebert, T., Allemand, T., & Toubiana, H. (2023). Stimulated noise and surface wave interferometry processing for hybrid seismic imaging. In *Stimulated noise and surface wave interferometry processing for hybrid seismic imaging* (Vol. 2023, p. 1–5). European Association of Geoscientists and Engineers. https://doi.org/10.3997/2214-4609.202320206

Bardainne, T., Vivin, L., & Tarnus, R. (2023). Railway near-surface passive seismic using trains as sources and fiber optic monitoring. In *Railway near-surface passive seismic using trains as sources and fiber optic monitoring* (Vol. 2023, p. 1–5). European Association of Geoscientists and Engineers. https://doi.org/10.3997/2214-4609.202320093

Bensen, G. D., Ritzwoller, M. H., Barmin, M. P., Levshin, A. L., Lin, F., Moschetti, M. P., et al. (2007). Processing seismic ambient noise data to obtain reliable broad-band surface wave dispersion measurements. *Geophysical Journal International*, *169*(3), 1239–1260. https://doi.org/10.1111/j.1365-246X.2007.03374.x

Bergamo, P., Boiero, D., & Socco, L. V. (2012). Retrieving 2D structures from surface-wave data by means of space-varying spatial windowing. *Geophysics*, *77*(4), EN39–EN51. https://doi.org/10.1190/geo2012-0031.1

Bergamo, P., Dashwood, B., Uhlemann, S., Swift, R., Chambers, J., Gunn, D., & Donohue, S. (2016). Time-lapse monitoring of climate effects on earthworks using surface waves. *Geophysics*, *81*(2), EN1–EN15. https://doi.org/10.1190/GEO2015-0275.1

Biot, M. A. (1956a). Theory of propagation of elastic waves in a fluid-saturated porous solid. II. Higher frequency range. *Journal of the Acoustical Society of America*, *28*(2), 179–191. https://doi.org/10.1121/1.1908241

Biot, M. A. (1956b). Theory of propagation of elastic waves in a fluid-saturated porous solid. I. Low-frequency range. *Journal of the Acoustical Society of America*, *28*(2), 168–178. https://doi.org/10.1121/1.1908239

Bohlen, T., Kugler, S., Klein, G., & Theilen, F. (2004). 1.5D inversion of lateral variation of Scholte-wave dispersion. *Geophysics*, *69*(22), 330–344. https://doi.org/10.1190/1.1707052

Boucher, M.-A., Quilty, J., & Adamowski, J. (2020). Data assimilation for streamflow forecasting using extreme learning machines and multilayer perceptrons. *Water Resources Research*, *56*(6), e2019WR026226. https://doi.org/10.1029/2019WR026226

Burzawa, A., Bodet, L., Dhemaied, A., Dangeard, M., Pasquet, S., Vitale, Q., et al. (2023). Detecting mechanical property anomalies along railway earthworks by Bayesian appraisal of MASW data. *Construction and Building Materials*, *404*, 133224. https://doi.org/10.1016/j.conbuildmat.2023.133224

Cai, H., Liu, S., Shi, H., Zhou, Z., Jiang, S., & Babovic, V. (2022). Toward improved lumped groundwater level predictions at catchment scale: Mutual integration of water balance mechanism and deep learning method. *Journal of Hydrology*, *613*, 128495. https://doi.org/10.1016/j.jhydrol.2022.128495

Cheng, F., Xia, J., Behm, M., Hu, Y., & Pang, J. (2019). Automated data selection in the Tau–*p* domain: Application to passive surface wave imaging. *Surveys in Geophysics*, *40*(5), 1211–1228. https://doi.org/10.1007/s10712-019-09530-2

Cheng, F., Xia, J., Luo, Y., Xu, Z., Wang, L., Shen, C., et al. (2016). Multichannel analysis of passive surface waves based on crosscorrelations. *Geophysics*, *81*(5), EN57–EN66. https://doi.org/10.1190/geo2015-0505.1

Cheng, F., Xia, J., Xu, Y., Xu, Z., & Pan, Y. (2015). A new passive seismic method based on seismic interferometry and multichannel analysis of surface waves. *Journal of Applied Geophysics*, *117*, 126–135. https://doi.org/10.1016/j.jappgeo.2015.04.005

Cheng, F., Xia, J., Xu, Z., Hu, Y., & Mi, B. (2018). Frequency–wavenumber (FK)-based data selection in high-frequency passive surface wave survey. *Surveys in Geophysics*, *39*(4), 661–682. https://doi.org/10.1007/s10712-018-9473-3

Chollet, F. E. A. (2015). Keras. https://keras.io

Clements, T., & Denolle, M. A. (2018). Tracking groundwater levels using the ambient seismic field. *Geophysical Research Letters*, *45*(13), 6459–6465. https://doi.org/10.1029/2018GL077706

Cunha Teixeira, J. (2024). Physics-guided deep learning model for daily groundwater table maps estimation using passive surface-wave dispersion [Dataset] [Software]. *Zenodo*. https://doi.org/10.5281/zenodo.10854339

Czarny, R., Zhu, T., & Shen, J. (2023). Spatiotemporal evaluation of Raleigh surface wave estimated from roadside dark fiber das array and traffic noise. *Seismica*, *2*(22). https://doi.org/10.26443/seismica.v2i2.247

Dafflon, B., Irving, J., & Holliger, K. (2009). Use of high-resolution geophysical data to characterize heterogeneous aquifers: Influence of data integration method on hydrological predictions. *Water Resources Research*, *45*(9), W09407. https://doi.org/10.1029/2008WR007646

Dagan, G. (1982). Stochastic modeling of groundwater flow by unconditional and conditional probabilities: 1. Conditional simulation and the direct problem. *Water Resources Research*, *18*(4), 813–833. https://doi.org/10.1029/WR018i004p00813

Dangeard, M., Rivière, A., Bodet, L., Schneider, S., Guérin, R., Jougnot, D., & Maineult, A. (2021). River corridor model constrained by time-lapse seismic acquisition. *Water Resources Research*, *57*(10), e2020WR028911. https://doi.org/10.1029/2020WR028911

Derode, A., Larose, E., Tanter, M., de Rosny, J., Tourin, A., Campillo, M., & Fink, M. (2003). Recovering the green's function from field-field correlations in an open scattering medium (l). *Journal of the Acoustical Society of America*, *113*(6), 2973–2976. https://doi.org/10.1121/1.1570436

Foti, S., Hollender, F., Garofalo, F., Albarello, D., Asten, M., Bard, P.-Y., et al. (2018). Guidelines for the good practice of surface wave analysis: A product of the interpacific project. *Bulletin of Earthquake Engineering*, *16*(6), 2367–2420. https://doi.org/10.1007/s10518-017-0206-7

Garambois, S., Sénéchal, P., & Perroud, H. (2002). On the use of combined geophysical methods to assess water content and water conductivity of near-surface formations. *Journal of Hydrology*, *259*(1–4), 32–48. https://doi.org/10.1016/s0022-1694(01)00588-1

Garambois, S., Voisin, C., Romero Guzman, M. A., Brito, D., Guillier, B., & Réfloch, A. (2019). Analysis of ballistic waves in seismic noise monitoring of water table variations in a water field site: Added value from numerical modelling to data understanding. *Geophysical Journal International*, *219*(3), 1636–1647. https://doi.org/10.1093/gji/ggz391

Gaubert-Bastide, T., Garambois, S., Bordes, C., Voisin, C., Oxarango, L., Brito, D., & Roux, P. (2022). High-resolution monitoring of controlled water table variations from dense seismic-noise acquisitions. *Water Resources Research*, *58*(8), e2021WR030680. https://doi.org/10.1029/2021WR030680

Goodfellow, I., Bengio, Y., & Courville, A. (2016). *Deep learning*. MIT Press.

Grêt, A., Snieder, R., & Scales, J. (2006). Time-lapse monitoring of rock properties with coda wave interferometry. *Journal of Geophysical Research*, *111*(B3), B03305. https://doi.org/10.1029/2004JB003354

Gutiérrez, F., Parise, M., De Waele, J., & Jourde, H. (2014). A review on natural and human-induced geohazards and impacts in karst. *Earth-Science Reviews*, *138*, 61–88. https://doi.org/10.1016/j.earscirev.2014.08.002

Hermans, T., Goderniaux, P., Jougnot, D., Fleckenstein, J. H., Brunner, P., Nguyen, F., et al. (2023). Advancing measurements and representations of subsurface heterogeneity and dynamic processes: Towards 4D hydrogeology. *Hydrology and Earth System Sciences*, *27*(1), 255–287. https://doi.org/10.5194/hess-27-255-2023

Jougnot, D., Linde, N., Haarder, E., & Looms, M. (2015). Monitoring of saline tracer movement with vertically distributed self-potential measurements at the HOBE agricultural site, Voulund, Denmark. *Journal of Hydrology*, *521*, 314–327. https://doi.org/10.1016/j.jhydrol.2014.11.041

Kawo, N. S., Korus, J., Kishawi, Y., Haacker, E. M. K., & Mittelstet, A. R. (2024). Three-dimensional probabilistic hydrofacies modeling using machine learning. *Water Resources Research*, *60*(7), e2023WR035910. https://doi.org/10.1029/2023WR035910

Kim, D., & Lekic, V. (2019). Groundwater variations from autocorrelation and receiver functions. *Geophysical Research Letters*, *46*(23), 13722–13729. https://doi.org/10.1029/2019GL084719

Kingma, D. P., & Ba, J. (2017). Adam: A method for stochastic optimization. https://doi.org/10.48550/arXiv.1412.6980

Kleinhans, M. G. (2005). Flow discharge and sediment transport models for estimating a minimum timescale of hydrological activity and channel and delta formation on mars. *Journal of Geophysical Research*, *110*(E12), E12003. https://doi.org/10.1029/2005JE002521

Klotzsche, A., Jonard, F., Looms, M., van der Kruk, J., & Huisman, J. (2018). Measuring soil water content with ground penetrating radar: A decade of progress. *Vadose Zone Journal*, *17*(1), 180052–180059. https://doi.org/10.2136/vzj2018.03.0052

Larose, E., Carrière, S., Voisin, C., Bottelin, P., Baillet, L., Guéguen, P., et al. (2015). Environmental seismology: What can we learn on earth surface processes with ambient noise? *Journal of Applied Geophysics*, *116*, 62–74. https://doi.org/10.1016/j.jappgeo.2015.02.001

Lecocq, T., Longuevergne, L., Pedersen, H., Brenguier, F., & Stammler, K. (2017). Monitoring ground water storage at mesoscale using seismic noise: 30 years of continuous observation and thermo-elastic and hydrological modeling. *Scientific Reports*, *7*(1), 14241. https://doi.org/10.1038/s41598-017-14468-9

Linnainmaa, S. (1976). Taylor expansion of the accumulated rounding error. *BIT Numerical Mathematics*, *16*(2), 146–160. https://doi.org/10.1007/BF01931367

Loeffler, O. H., & Bano, M. (2004). Ground penetrating radar measurements in a controlled vadose zone: Influence of the water content. *Vadose Zone Journal*, *3*(4), 1082–1092. https://doi.org/10.2113/3.4.1082

Lu, Z. (2014). Feasibility of using a seismic surface wave method to study seasonal and weather effects on shallow surface soils. *Journal of Environmental & Engineering Geophysics*, *19*(2), 71–85. https://doi.org/10.2113/JEEG19.2.71

Maillot, M., Flipo, N., Rivière, A., Desassis, N., Renard, D., Goblet, P., & Vincent, M. (2019). Technical note: Water table mapping accounting for river–aquifer connectivity and human pressure. *Hydrology and Earth System Sciences*, *23*(11), 4835–4849. https://doi.org/10.5194/hess-23-4835-2019

Mao, S., Lecointre, A., van der Hilst, R., & Campillo, M. (2022). Space-time monitoring of groundwater fluctuations with passive seismic interferometry. *Nature Communications*, *13*(1), 4643. https://doi.org/10.1038/s41467-022-32194-3

Mi, B., Xia, J., Tian, G., Shi, Z., Xing, H., Chang, X., et al. (2022). Near-surface imaging from traffic-induced surface waves with dense linear arrays: An application in the urban area of Hangzhou, China. *Geophysics*, *87*(2), B145–B158. https://doi.org/10.1190/geo2021-0184.1

Mi, B., Xia, J., Xu, Y., You, B., & Chen, Y. (2023). Retrieval of surface waves from high-speed-train-induced vibrations using seismic interferometry. *Geophysics*, *88*(5), KS113–KS126. https://doi.org/10.1190/geo2022-0603.1

Murtagh, F. (1991). Multilayer perceptrons for classification and regression. *Neurocomputing*, *2*(5), 183–197. https://doi.org/10.1016/0925-2312(91)90023-5

Nazarian, S., Stokoe, K., & Hudson, W. (1983). Use of spectral analysis of surface waves method for determination of moduli and thicknesses of pavement systems. *Transportation Research Record*.

Nguyen-Thé, D., Ollagnier, S., Pétrignet, M., Thonnon, J., & Joannes, O. (2010). Carte piézométrique de la nappe des grès du Trias inférieur de 2010. Report BRGM/RP-59294-FR. Retrieved from https://infoterre.brgm.fr/rapports/RP-59294-FR.pdf

Ning, L., Xia, J., Dai, T., Liu, Y., Zhang, H., & Xi, C. (2022). High-frequency surface-wave imaging from traffic-induced noise by selecting inline sources. *Surveys in Geophysics*, *43*(6), 1873–1899. https://doi.org/10.1007/s10712-022-09723-2

O'Neill, A., & Matsuoka, T. (2005). Dominant higher surface-wave modes and possible inversion pitfalls. *Journal of Environmental & Engineering Geophysics*, *10*(2), 185–201. https://doi.org/10.2113/JEEG10.2.185

Panda, S., Kumar, S., Pradhan, S., Sidhu, J., Kralia, A., & Thakur, D. M. (2022). Effect of groundwater table fluctuation on slope instability: A comprehensive 3D simulation approach for Kotropi landslide, India. *Landslides*, *20*(3), 663–682. https://doi.org/10.1007/s10346-022-01993-6

Parise, M. (2019). Sinkholes. In W. B. White, D. C. Culver, & T. Pipan (Eds.), *Encyclopedia of caves* (3rd ed., pp. 934–942). Academic Press. https://doi.org/10.1016/B978-0-12-814124-3.00110-2

Park, C. B., & Miller, R. D. (2008). Roadside passive multichannel analysis of surface waves (MASW). *Journal of Environmental & Engineering Geophysics*, *13*(1), 1–11. https://doi.org/10.2113/JEEG13.1.1

Park, C. B., Miller, R. D., & Xia, J. (1999). Multichannel analysis of surface waves. *Geophysics*, *64*(3), 800–808. https://doi.org/10.1190/1.1444590

Pasquet, S., & Bodet, L. (2017). SWIP: An integrated workflow for surface-wave dispersion inversion and profiling. *Geophysics*, *82*(6), WB47–WB61. https://doi.org/10.1190/geo2016-0625.1

Pasquet, S., Bodet, L., Dhemaied, A., Mouhri, A., Vitale, Q., Rejiba, F., et al. (2015). Detecting different water table levels in a shallow aquifer with combined P-surface and SH-wave surveys: Insights from VP/VS or Poisson's ratios. *Journal of Applied Geophysics*, *113*, 38–50. https://doi.org/10.1016/j.jappgeo.2014.12.005

Pasquet, S., Bodet, L., Longuevergne, L., Dhemaied, A., Camerlynck, C., Rejiba, F., & Guérin, R. (2015). 2D characterization of near-surface VP/VS: Surface-wave dispersion inversion versus refraction tomography. *Near Surface Geophysics*, *13*(4), 315–332. https://doi.org/10.3997/1873-0604.2015028

Qin, L., Steidl, J. H., Qiu, H., Nakata, N., & Ben-Zion, Y. (2022). Monitoring seasonal shear wave velocity changes in the top 6 m at garner valley in southern California with borehole data. *Geophysical Research Letters*, *49*(23), e2022GL101189. https://doi.org/10.1029/2022GL101189

Quiros, D. A., Brown, L. D., & Kim, D. (2016). Seismic interferometry of railroad induced ground motions: Body and surface wave imaging. *Geophysical Journal International*, *205*(1), 301–313. https://doi.org/10.1093/gji/ggw033

Rahardjo, H., Satyanaga, A., Leong, E., & Ng, Y. (2010). Effects of groundwater table position and soil properties on stability of slope during rainfall. *Journal of Geotechnical and Geoenvironmental Engineering*, *136*(11), 1555–1564. https://doi.org/10.1061/(ASCE)GT.1943-5606.0000385

Rebert, T., Allemand, T., Bardainne, T., Cai, C., & Chauris, H. (2023). Seismic emissions from a passing train: Turning ambient noise into a controlled source. In *EGU general assembly conference abstracts* (p. EGU-7289). https://doi.org/10.5194/egusphere-egu23-7289

Rebert, T., Bardainne, T., Allemand, T., Cai, C., & Chauris, H. (2024). Characterization of train kinematics and source wavelets from near-field seismic data. *Geophysical Journal International*, *237*(2), 697–715. https://doi.org/10.1093/gji/ggae067

Rebert, T., Bardainne, T., Cai, C., Allemand, T., & Chauris, H. (2024). Matched field processing of train vibrations for opportunistic surface wave tomography. In *EGU general assembly conference abstracts* (p. 18405). https://doi.org/10.5194/egusphere-egu24-18405

Rezaeifar, M., Lavoué, F., Maggio, G., Xu, Y., Bean, C. J., Pinzon-Rincon, L., et al. (2023). Imaging shallow structures using interferometry of seismic body waves generated by train traffic. *Geophysical Journal International*, *233*(2), 964–977. https://doi.org/10.1093/gji/ggac507

Rosenblatt, F. (1958). The perceptron: A probabilistic model for information storage and organization in the brain. *Psychological Review*, *65*(6), 386–408. https://doi.org/10.1037/h0042519

Sambridge, M. (1999). Geophysical inversion with a neighbourhood algorithm—I. Searching a parameter space. *Geophysical Journal International*, *138*(2), 479–494. https://doi.org/10.1046/j.1365-246X.1999.00876.x

Samouëlian, A., Cousin, I., Tabbagh, A., Bruand, A., & Richard, G. (2005). Electrical resistivity survey in soil science: A review. *Soil and Tillage Research*, *83*(2), 173–193. https://doi.org/10.1016/j.still.2004.10.004

Shorten, C., & Khoshgoftaar, T. M. (2019). A survey on image data augmentation for deep learning. *Journal of Big Data*, *6*(1), 60. https://doi.org/10.1186/s40537-019-0197-0

Socco, L., & Strobbia, C. (2004). Surface-wave method for near-surface characterization: A tutorial. *Near Surface Geophysics*, *2*(4), 165–185. https://doi.org/10.3997/1873-0604.2004015

Socco, L. V., Foti, S., & Boiero, D. (2010). Surface-wave analysis for building near-surface velocity models—Established approaches and new perspectives. *Geophysics*, *75*(5), 75A83–75A102. https://doi.org/10.1190/1.3479491

Solazzi, S. G., Bodet, L., Holliger, K., & Jougnot, D. (2021). Surface-wave dispersion in partially saturated soils: The role of capillary forces. *Journal of Geophysical Research: Solid Earth*, *126*(12), e2021JB022074. https://doi.org/10.1029/2021JB022074

Tarnus, R., Bardainne, T., Michel, L., Deladerrière, N., & Cai, C. (2022a). A case study for railway underground imaging using trains as seismic signal for sinkhole and subsidence phenomena prevention. In *Fifth international conference on railway technology: Research, development and maintenance* (Vol. 1, p. 13). https://doi.org/10.4203/ccc.1.10.13

Tarnus, R., Bardainne, T., Michel, L., Deladerriere, N., Cai, C., Hallier, A., & Boisson-Gaboriau, J. (2022b). A case study for underground imaging using trains as seismic signal to investigate subsidence phenomena. In *A case study for underground imaging using trains as seismic signal to investigate subsidence phenomena* (Vol. 2022, p. 1–5). European Association of Geoscientists and Engineers. https://doi.org/10.3997/2214-4609.202220033

Tripathy, K., & Mishra, A. (2024). Deep learning in hydrology and water resources disciplines: Concepts, methods, applications, and research directions. *Journal of Hydrology*, *628*, 130458. https://doi.org/10.1016/j.jhydrol.2023.130458

Tsai, F. T.-C., & Li, X. (2008). Inverse groundwater modeling for hydraulic conductivity estimation using Bayesian model averaging and variance window. *Water Resources Research*, *44*(9), W09434. https://doi.org/10.1029/2007WR006576

Voisin, C., Garambois, S., Massey, C., & Brossier, R. (2016). Seismic noise monitoring of the water table in a deep-seated, slow-moving landslide. *Interpretation*, *4*(3), SJ67–SJ76. https://doi.org/10.1190/INT-2016-0010.1

Voisin, C., Guzmán, M., Réfloch, A., Taruselli, M., & Garambois, S. (2017). Groundwater monitoring with passive seismic interferometry. *Journal of Water Resource and Protection*, *9*(12), 1414–1427. https://doi.org/10.4236/jwarp.2017.912091

Waltham, T., Bell, F., & Culshaw, M. (2004). *Sinkholes and subsidence: Karst and cavernous rocks in engineering and construction* (2005th ed.). Springer. https://doi.org/10.1007/b138363

Wapenaar, K. (2004). Retrieving the elastodynamic Green's function of an arbitrary inhomogeneous medium by cross correlation. *Physical Review Letters*, *93*(25), 254301. https://doi.org/10.1103/PhysRevLett.93.254301

Wapenaar, K., Draganov, D., Snieder, R., Campman, X., & Verdel, A. (2010). Tutorial on seismic interferometry. Part I: Basic principles and applications. *Geophysics*, *75*, 75A195–75209. https://doi.org/10.1190/1.3457445

Wapenaar, K., Slob, E., Snieder, R., & Curtis, A. (2010). Tutorial on seismic interferometry: Part 2—Underlying theory and new advances. *Geophysics*, *75*(5), 75A211–75227. https://doi.org/10.1190/1.3463440

Wathelet, M. (2008). An improved neighborhood algorithm: Parameter conditions and dynamic scaling. *Geophysical Research Letters*, *35*(9), L09301. https://doi.org/10.1029/2008GL033256

Weaver, R. L., & Lobkis, O. I. (2004). Diffuse fields in open systems and the emergence of the Green's function (l). *Journal of the Acoustical Society of America*, *116*(5), 2731–2734. https://doi.org/10.1121/1.1810232

Werbos, P. J. (1982). Applications of advances in nonlinear sensitivity analysis. In R. F. Drenick, & F. Kozin (Eds.), *System modeling and optimization* (pp. 762–770). Springer Berlin Heidelberg.

Whiteley, J., Chambers, J., Uhlemann, S., Boyd, J., Cimpoiasu, M., Holmes, J., et al. (2020). Landslide monitoring using seismic refraction tomography—The importance of incorporating topographic variations. *Engineering Geology*, *268*, 105525. https://doi.org/10.1016/j.enggeo.2020.105525

Xiao, X., Gutiérrez, F., & Guerrero, J. (2020). The impact of groundwater drawdown and vacuum pressure on sinkhole development. Physical laboratory models. *Engineering Geology*, *279*, 105894. https://doi.org/10.1016/j.enggeo.2020.105894

Ying, X. (2019). An overview of overfitting and its solutions. *Journal of Physics: Conference Series*, *1168*, 022022. https://doi.org/10.1088/1742-6596/1168/2/022022

You, B., Mi, B., Guan, B., Zhang, H., & Liu, Y. (2023). High-quality surface wave retrieval from vibrations generated by high-speed trains moving on viaducts. *Journal of Applied Geophysics*, *212*, 105005. https://doi.org/10.1016/j.jappgeo.2023.105005

Zhang, C., Brodeur, Z. P., Steinschneider, S., & Herman, J. D. (2022). Leveraging spatial patterns in precipitation forecasts using deep learning to support regional water management. *Water Resources Research*, *58*(9), e2021WR031910. https://doi.org/10.1029/2021WR031910

Zhang, S., Luo, B., Ben-Zion, Y., Lumley, D. E., & Zhu, H. (2023). Monitoring terrestrial water storage, drought and seasonal changes in central Oklahoma with ambient seismic noise. *Geophysical Research Letters*, *50*(17), e2023GL103419. https://doi.org/10.1029/2023GL103419